Flagellated bacteria swim in circles near a rigid wall

Yunyoung Park
Innovation Center for Industrial Mathematics, National Institute for Mathematical Sciences, Yeongtonggu, Suwon, Gyeonggi, 16229, Republic of Korea

Yongsam Kim*
Department of Mathematics, Chung-Ang University, Dongjakgu, Heukseokdong, Seoul, 156-756, Republic of Korea

Sookkyung Lim†
Department of Mathematical Sciences, University of Cincinnati, 4199 French Hall West, Cincinnati, Ohio 45221, USA

(Received 1 August 2019; revised manuscript received 6 November 2019; published 30 December 2019)

The rotation of bacterial flagella driven by rotary motors enables the cell to swim through fluid. Bacteria run and reorient by changing the rotational direction of the motor for survival. Fluid environmental conditions also change the course of swimming; for example, cells near a solid boundary draw circular trajectories rather than straight runs. We present a bacterium model with a single flagellum that is attached to the cell body and investigate the effect of the solid wall on bacterial locomotion. The cell body of the bacterium is considered to be a rigid body and is linked via a rotary motor to the elastic flagellum which is modeled by the Kirchhoff rod theory. The hydrodynamic interaction of the cell near a solid boundary is described using the regularized Stokes formulation combined with the image system. We show that the trajectories of the bacteria near a solid boundary are influenced by the rotation rate of the motor, the shape of the cell body, helical geometry, and elastic properties of the flagellum.

DOI: 10.1103/PhysRevE.100.063112

I. INTRODUCTION

Flagellated microorganisms are propelled by rotating their flagellar motors that are embedded in the cell membrane. The rotation of each motor is transmitted to the flagellar filament via a flexible hook, resulting in the rotation of the flagellum so that the cells can swim [1–9]. Flagellated bacteria run forward or backward by a unidirectional rotation of the motors; however, they can reorient by changing the rotational direction of the motor or by transforming the flagellar forms to survive in a fluid-filled environment.

In the absence of any environmental obstacles such as rigid walls, multi-flagellated bacteria such as *Escherichia coli* run approximately straight when all flagella form a left-handed helical bundle while keeping all motors spinning counterclockwise (CCW). However, *E. coli* cells take clockwise circular trajectories when they swim near rigid surfaces [10–12]. It has been observed that bacteria swim toward the rigid surface to be entrapped nearby, which is crucial for the initiation of biofilm formation [13–15]. The trajectory drawn by the cell entrapped near the surface was found to be circular, as is commonly observed under the microscope [11,12,16]. It is also reported that a single-flagellated bacterium *Vibrio alginolyticus* swims in circles near a surface [17,18].

Bacterial swimming near a no-slip planar wall was analyzed as early as 1965 by Reynolds [19], who considered the swimmer as an infinite waving sheet. Ramia *et al.* [7] employed the boundary element method to describe the hydrodynamics of bacteria near a planar wall, showing that when it swims close to a solid boundary, the swimmer exhibits a circular motion. Lauga *et al.* [20] investigated experimentally and numerically the motion of an *E. coli* bacterium near a solid wall by employing resistive force theory. They also found a circular clockwise rotation of bacteria with a good agreement in experimental and computational results. Both computational models in Refs. [7,20] take the form of a spherical shape of the cell body, whereas a very common shape of the cell body is a prolate spheroid. Giacché *et al.* [16] further investigated the hydrodynamic trapping mechanism focusing on the correlation between the radii of circular trajectories and the separation gap from the surface as the aspect ratio of the cell body and the flagellar geometry are varied. Shum *et al.* [21] investigated the near-wall bacterial locomotion under various geometrical conditions of the cell body and the flagellum and found an optimal condition for power efficiency. However, their flagellum is modeled as a rigidly rotating body although actual flagella exhibit elastic properties such as polymorphic transformations [5,22–24].

In this paper we use a comprehensive model for a freely swimming monotrichous bacterium including a cell body and a flexible helical flagellum equipped with a motor to investigate the swimming motion of a single-flagellated bacterium near a solid planar wall and to explore the dependence of its

*Corresponding author: kimy@cau.ac.kr
†Corresponding author: sookkyung.lim@uc.edu

 ©2019 American Physical Society

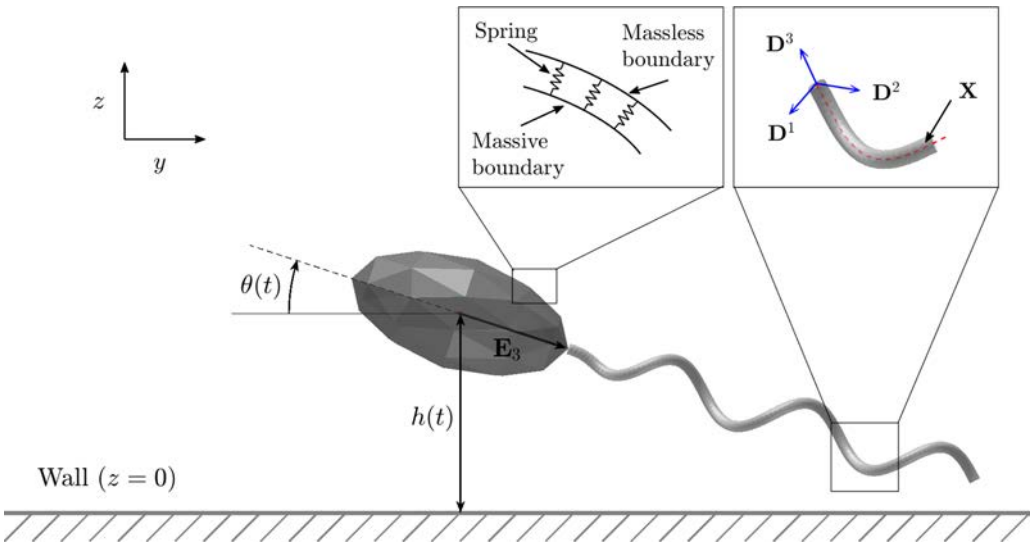

FIG. 1. A schematic view of a single-flagellated bacterium near a rigid planar wall located at $z = 0$. The flagellum of the cell is represented by a space curve $\mathbf{X}$ and its associated orthonormal triad $\{\mathbf{D}^1, \mathbf{D}^2, \mathbf{D}^3\}$. The surface of the spheroidal cell body is represented by two Lagrangian descriptions: $\mathbf{X}_b$ as a massless boundary and $\mathbf{Y}_b$ as a massive boundary. The distance between the center of mass of the cell body and the wall is denoted by $h(t)$, and the inclination angle between the major axis of the cell body ($-\mathbf{E}_3$) from the $z = 0$ plane is denoted by $\theta(t)$ at time t.

swimming pattern on various physical parameters such as the shape of the cell body, the helical geometry, and the elastic properties of the flagellum and the rotational frequency of the motor. Here a single flagellum can also be interpreted as a flagellar bundle in *E. coli* bacteria when they take a forward run.

The mathematical model of a single-flagellated bacterium for the present study consists of a cell body and a helical flagellum that share a motor at a junction. We describe the elastic flagellar filament as a space curve associated with orthonormal triads that measure the amount of bending and twisting along the rod, which is based on the Kirchhoff rod theory [25–27]. The penalty idea [28] is used to model the cell body as a rigid body that can translate and rotate as a whole. Unlike the general mathematical models used in previous studies [7,20,21], we do not impose the time evolution (velocity or position) of the rigidly rotating flagellum; instead, we rotate the motor only of which the torque is propagated along the flagellum, eventually resulting in the rotation of the whole flagellum. The cell body naturally counterrotates to balance the torque generated at the motor.

In order to investigate the hydrodynamic interaction of the cell near a solid boundary, we employ the method of image system of the regularized Stokes formulation which was introduced by Cortez *et al.* [29,30]. Whereas the method proposed in Refs. [29,30] computes the linear velocity of fluid with no-slip boundary given external force and torque, our model further requires one to compute the angular velocity to rotate the triads of the flagella. We provide the explicit form of the angular velocity, which is obtained by taking the curl of the linear velocity and its detailed computational recipe.

II. MATHEMATICAL MODEL

A mathematical model of a single-flagellated bacterium consists of a spheroidal cell body and a helical flagellum, whose one end is attached to the cell membrane. See Fig. 1 for the schematic diagram of a cell in the presence of the solid planar wall. The flagellum is a long-thin filament and thus can be described with Kirchhoff rod theory [25]. The cell body can be described as a rigid body using the penalty method [28,31], and the hydrodynamic interaction of the bacterium can be described by the regularized Stokes formulation [26,29,30].

The Kirchhoff rod representation for the flagellum is a space curve $\mathbf{X}(s,t)$ together with its associated orthonormal triad $\{\mathbf{D}^1(s,t), \mathbf{D}^2(s,t), \mathbf{D}^3(s,t)\}$ along the curve, in which the curve describes the centerline of the flagellum and the triad measures the amount of bending and twisting of the flagellum. Here t is time and s is a Lagrangian coordinate with $0 \leqslant s \leqslant L$, where L is the length of the helical flagellum. The initial shape of the helical centerline $\mathbf{X}(s,0)$ is described as follows [32]:

$$\mathbf{X}(s,0) = (r(s)\cos(\alpha s), r(s)\sin(\alpha s), s), \tag{1}$$

where α is the wave number and the helical radius $r(s)$ is a variable function defined as

$$r(s) = r_0(1 - e^{-ks^2}) \quad \text{for} \quad 0 \leqslant s \leqslant L, \tag{2}$$

where k is a constant that determines how rapidly the helix reaches its maximal radius. The helical radius increases gradually to be r_0 for the helical flagellum. For the orthonormal triad, the vector $\mathbf{D}^3(s,0)$ is initially defined as a unit tangent vector to the curve $\mathbf{X}(s,0)$, and the other two vectors, $\mathbf{D}^1(s,0)$ and $\mathbf{D}^2(s,0)$, are normal and binormal vectors. Note that the initial configuration of the helical flagellum is at rest, and its deformation causes elastic restoring force to the reference configuration.

The cell body is built as a hollow spheroid which is represented by two Lagrangian descriptions: one is a massless surface denoted by $\mathbf{X}_b(q,r,t)$ which interacts directly with the surrounding fluid, and the other is a massive one denoted by $\mathbf{Y}_b(q,r,t)$ which carries all of the mass, where (q,r)

designates points on a rectangle Γ. These two descriptions are supposed to be the same body and thus linked by a system of stiff springs with 0 rest length. The massive surface $\mathbf{Y}_\mathrm{b}(q,r,t)$ has no direct interaction with the fluid and moves as a rigid body in a vacuum, with the only forces and torques applied on the body being the forces generated from the springs that connect the massless description to the massive description of the rigid body. Mathematical formulation for the dynamics of the two descriptions $\mathbf{X}_\mathrm{b}(q,r,t)$ and $\mathbf{Y}_\mathrm{b}(q,r,t)$ for the rigid cell body will be described in detail below.

We now state a coupled system of fluid-structure interaction equations for a swimming bacterium in a viscous incompressible fluid as follows:

$$0 = -\nabla p + \mu\Delta\mathbf{u} + \mathbf{g}, \quad 0 = \nabla\cdot\mathbf{u}, \tag{3}$$

$$0 = \mathbf{f} + \frac{\partial\mathbf{F}}{\partial s}, \quad 0 = \mathbf{n} + \frac{\partial\mathbf{N}}{\partial s} + \left(\frac{\partial\mathbf{X}}{\partial s}\times\mathbf{F}\right), \tag{4}$$

$$\mathbf{F}_\mathrm{b}(q,r,t) = K_\mathrm{b}[\mathbf{Y}_\mathrm{b}(q,r,t) - \mathbf{X}_\mathrm{b}(q,r,t)], \tag{5}$$

$$\begin{aligned}\mathbf{g}(\mathbf{x},t) = &\int_0^L [-\mathbf{f}(s,t)]\psi_\delta[\mathbf{x}-\mathbf{X}(s,t)]\,ds\\ &+\frac{1}{2}\nabla\times\int_0^L[-\mathbf{n}(s,t)]\psi_\delta[\mathbf{x}-\mathbf{X}(s,t)]\,ds\\ &+\int\mathbf{F}_\mathrm{b}(q,r,t)\psi_\delta[\mathbf{x}-\mathbf{X}_\mathrm{b}(q,r,t)]\,dq\,dr,\end{aligned} \tag{6}$$

$$\frac{\partial\mathbf{X}(s,t)}{\partial t} = \mathbf{u}(\mathbf{X}(s,t),t), \quad \frac{\partial\mathbf{X}_\mathrm{b}(q,r,t)}{\partial t} = \mathbf{u}(\mathbf{X}_\mathrm{b}(q,r,t),t), \tag{7}$$

$$\frac{\partial\mathbf{D}^i(s,t)}{\partial t} = \mathbf{w}(\mathbf{X}(s,t),t)\times\mathbf{D}^i(s,t), \quad i=1,2,3. \tag{8}$$

Equation (3) is the incompressible Stokes equations where μ is the fluid viscosity. The unknown variables as functions of the fixed Cartesian coordinates $\mathbf{x}$ and the time t are the fluid velocity $\mathbf{u}$, fluid pressure p, and external fluid force density $\mathbf{g}$. Equation (4) expresses the equations for force and torque balances where $\mathbf{F}(s,t)$ and $\mathbf{N}(s,t)$ are the force and moment, respectively, transmitted across a section of the rod at the Lagrangian coordinate s at time t, and $\mathbf{f}(s,t)$ and $\mathbf{n}(s,t)$ are the applied force and torque densities, respectively. The force and moment generated from the elastic flagellum can be expanded in the basis of the orthonormal triad and written as

$$\mathbf{F} = \sum_{i=1}^3 F_i\mathbf{D}^i, \quad \mathbf{N} = \sum_{i=1}^3 N_i\mathbf{D}^i, \tag{9}$$

with the following constitutive relations:

$$\begin{aligned}F_i &= b_i\left(\mathbf{D}^i\cdot\frac{\partial\mathbf{X}}{\partial s} - \delta_{3i}\right),\\ N_i &= a_i\left(\frac{\partial\mathbf{D}^j}{\partial s}\cdot\mathbf{D}^k - \Omega_i\right), \quad i=1,2,3,\end{aligned} \tag{10}$$

where δ_{3i} is the Kronecker delta and (i,j,k) is any cyclic permutation of (1,2,3). The constitutive relations can be derived from a variational argument of the elastic energy potential for the unconstrained version of the Kirchhoff rod [25]:

$$\begin{aligned}E = \frac{1}{2}\int_0^L\Bigg[&\sum_{i=1}^3 a_i\left(\frac{\partial\mathbf{D}^j}{\partial s}\cdot\mathbf{D}^k - \Omega_i\right)^2\\ &+\sum_{i=1}^3 b_i\left(\mathbf{D}^i\cdot\frac{\partial\mathbf{X}}{\partial s} - \delta_{3i}\right)^2\Bigg]ds.\end{aligned} \tag{11}$$

Here the coefficients a_1 and a_2 are the bending moduli, a_3 is the twist modulus of the rod, b_1 and b_2 are the shear moduli, and b_3 is the stretching modulus. The strain twist vector $(\Omega_1,\Omega_2,\Omega_3)$ indicates the intrinsic property of the elastic rod in which $\kappa \equiv \sqrt{\Omega_1^2+\Omega_2^2}$ is the intrinsic curvature and Ω_3 is the intrinsic twist of the rod of which the negative values determine a left-handed helix and positive values determine a right-handed helix. The flagellum in this work is assumed to be left-handed.

In Eq. (5), $\mathbf{F}_\mathrm{b}$ is the restoring force acting on the massless boundary $\mathbf{X}_\mathrm{b}$. Since the massless and massive descriptions are supposed to represent the same body, when a pair of corresponding boundary points moves apart, a restoring force $\mathbf{F}_\mathrm{b}$ comes into play to constrain them to stay close for a sufficiently large penalty constant K_b. According to Newton's third law, the negative force density $-\mathbf{F}_\mathrm{b}$ acts upon the massive rigid body $\mathbf{Y}_\mathrm{b}$; see Eqs. (15) and (16) below.

Equation (6) is the interaction equation between the force densities of the bacterium and fluid, in which the fluid force density $\mathbf{g}$, exerted by the bacterium boundary, consists of three terms; the first two terms represent the force and torque from the elastic flagellum, and the last term represents the force from the surface of the cell body. The blob (cutoff) function ψ_δ is defined as

$$\psi_\delta(\mathbf{r}) = \frac{15\delta^4}{8\pi(|\mathbf{r}|^2+\delta^2)^{7/2}}, \tag{12}$$

where δ is the regularization parameter and $\mathbf{r} = \mathbf{x}-\mathbf{X}$ (or $\mathbf{r} = \mathbf{x}-\mathbf{X}_\mathrm{b}$) for a point $\mathbf{x}$ in the fluid and a point $\mathbf{X}$ (or $\mathbf{X}_\mathrm{b}$) on the cell [26,33]. The blob function ψ_δ is a radially symmetric bell-shaped curve with infinite support, spreading most of the force and moment within a ball with the radius δ and the center at the boundary point $\mathbf{X}$ (or $\mathbf{X}_\mathrm{b}$) and satisfying $\iiint_{\mathbb{R}^3}\psi_\delta(\mathbf{r})\,d\mathbf{r} = 1$. Equations (7) and (8) are the no-slip conditions for the linear and angular velocities of the cell, respectively, where $\mathbf{w} = \frac{1}{2}\nabla\times\mathbf{u}(\mathbf{x},t)$ is the fluid angular velocity.

In order to describe the translation and rotation of the rigid cell body $\mathbf{Y}_\mathrm{b}(q,r,t)$, we let $\mathbf{Y}_\mathrm{cm}(t)$ be the center of mass of the cell body, and $\{\mathbf{E}_1(t),\mathbf{E}_2(t),\mathbf{E}_3(t)\}$ be the orthonormal basis for the coordinate system fixed to the body with its origin at the center of mass. Note that $\mathbf{E}_3(t)$ is in the direction of a major axis of the spheroidal cell body and points toward the motor point at the pole. Then the massive boundary can be written as

$$\mathbf{Y}_\mathrm{b}(q,r,t) = \mathbf{Y}_\mathrm{cm}(t) + \mathcal{E}(t)\mathbf{C}(q,r), \tag{13}$$

where $\mathcal{E}(t)$ is a 3×3 matrix of which the ith column is the 3×1 vector $\mathbf{E}_i(t)$, and $\mathbf{C}(q,r)$ is a 3×1 vector which represents the coordinates fixed to the cell body in this system and thus

is independent of time. Equations of motion for the rigid cell body $\mathbf{Y}_b(q, r, t)$ are now given by

$$\frac{d\mathbf{Y}_{cm}}{dt} = \mathbf{V}_{cm}(t), \tag{14}$$

$$M\frac{d\mathbf{V}_{cm}}{dt} = -\iint_\Gamma \mathbf{F}_b(q, r, t)\, dq\, dr, \tag{15}$$

$$\frac{d\mathbf{L}}{dt} = \iint_\Gamma [\mathbf{Y}_b(q, r, t) - \mathbf{Y}_{cm}(t)] \times [-\mathbf{F}_b(q, r, t)]\, dq\, dr, \tag{16}$$

$$\mathbf{\Omega}(t) = \mathcal{E}(t)\, I_0^{-1}\, \mathcal{E}(t)^T \mathbf{L}(t), \tag{17}$$

$$\frac{d\mathbf{E}_i}{dt} = \mathbf{\Omega}(t) \times \mathbf{E}_i(t), \quad i = 1, 2, 3. \tag{18}$$

Equations (14) and (15) describe the translational motion of the center of mass, where $\mathbf{V}_{cm}(t)$ is the velocity of the center of mass, and M is the total mass of the hollow cell body, which can be computed by $M = \iint_\Gamma m(q, r)\, dq\, dr$, where $m(q, r)$ is the mass density of the cell body. Equations (16) and (18) describe the rotational motion of the cell body about the center of mass, where $\mathbf{L}(t)$ and $\mathbf{\Omega}(t)$ are the angular momentum and the angular velocity of the cell body, respectively. The initial moment of inertial tensor, I_0, can be computed by $I_0 = \iint_\Gamma m(q, r)(\mathbf{C}^T\mathbf{C}I_3 - \mathbf{C}\mathbf{C}^T)\, dq\, dr$, where I_3 is 3×3 identity matrix. In summary, the cell body translates and rotates at the cost of the resultant forces and moments from the deviation of two Lagrangian descriptions for the cell body.

Finally, we complete this section by showing how we embed the filament into the cell body and how we rotate the motor. To do that, we first adopt two constraints: one is to attach the bottom end of the flagellum (representing the motor point) to the north pole of the cell body, and the other is to align the two directions of the flagellum at the motor point and the cell body. To achieve this, we define the feedback force and moment densities as follows:

$$\mathbf{f}_m(t) = K_1\big[\mathbf{Y}_b^m(t) - \mathbf{X}(0, t)\big], \tag{19}$$

$$\mathbf{n}_m(t) = K_2[\mathbf{E}_3(t) \times \mathbf{D}^3(0, t)], \tag{20}$$

where K_1 and K_2 are large constants, and $\mathbf{X}(0, t)$ and $\mathbf{Y}_b^m(t)$ represent the motor point of the flagellum and the north pole of the cell body, respectively. The force density $\mathbf{f}_m(t)$ acts on the motor point $\mathbf{X}(0, t)$, and the negative force density $-\mathbf{f}_m(t)$ acts on $\mathbf{Y}_b^m(t)$ and affects the total force and torque on the cell body. Similarly, the moment density $\mathbf{n}_m(t)$ and its negative value are applied to $\mathbf{X}(0, t)$ and $\mathbf{Y}_b^m(t)$, respectively. By the feedback mechanism with sufficiently large values of K_1 and K_2, $\mathbf{X}(0, t)$ stays close to $\mathbf{Y}_b^m(t)$, and the tangent vector $\mathbf{D}^3(0, t)$ at the motor point is aligned closely with the direction $\mathbf{E}_3(t)$ of the cell body.

The motor of the flagellum, represented by $\mathbf{X}(0, t)$, rotates at any given frequency ω about the tangent vector $\mathbf{D}^3(0, t)$. This can be done by defining the orthonormal triad at the motor point $\mathbf{X}(0, t)$ as follows:

$$\mathbf{D}^i(0, t) = \mathcal{R}[\mathbf{D}^3(0, t)]\mathbf{D}^i_{mot}(0, t), \quad i = 1, 2, \tag{21}$$

where $\mathcal{R}[\mathbf{D}^3(0, t)]$ represents a rotational matrix to transform the unit vector (0,0,1) to the unit vector $\mathbf{D}^3(0, t)$. The two orthonormal vectors $\mathbf{D}^i_{mot}(t)$, $i = 1, 2$, represent the vectors, which are rotated at frequency ω from the two standard basis (1,0,0) and (0,1,0), respectively:

$$\mathbf{D}^1_{mot}(t) = (\cos(2\pi\omega t), \sin(2\pi\omega t), 0),$$

$$\mathbf{D}^2_{mot}(t) = (-\sin(2\pi\omega t), \cos(2\pi\omega t), 0).$$

The twist generated by the rotary motor is transmitted along the flagellum to its free end, leading to the rotation of the helical filament, and the resultant countertorque at the rotating motor automatically appears to balance the torque so that the cell body counterrotates. See Ref. [31] for a more detailed description of mathematical formulation.

III. THE METHOD OF REGULARIZED IMAGE SYSTEM

In this section, we present the regularized Stokes formulation combined with the image system to compute the linear and angular velocities of fluid with a rigid wall. We consider an infinite plane wall ($z = 0$) at which the fluid velocity vanishes. In the presence of the external fluid force $\mathbf{g}$ resulting from the forces and toques of the immersed boundary (flagellum and cell body), the solution (the linear velocity) of Eq. (3) may not be zero on the wall. The idea of the method of image system is to define various fundamental solutions (kernels) such as stokeslet, potential dipole, rotlet, doublet, and quadrupole and rotlet doublet and to apply them to appropriate forces and torques at the image points of the immersed boundary so that the flow at the wall is at rest. The image system method was introduced by Cortez *et al.* [29,30] in order to apply the no-slip wall conditions for the linear velocity. Here we summarize both the linear and angular velocities in the image system and provide numerical schemes. The detailed derivation of the mathematical formulation will be described in the Appendix.

Given a point force $\mathbf{f}_0$ and a point torque $\mathbf{n}_0$ applied at a boundary point $\mathbf{X}_0$, we rewrite the Stokes equation in terms of the regularized force and torque as follows:

$$0 = -\nabla p + \mu\Delta\mathbf{u} + \mathbf{f}_0\psi_\delta(\mathbf{x} - \mathbf{X}_0) + \tfrac{1}{2}\nabla \times \mathbf{n}_0\psi_\delta(\mathbf{x} - \mathbf{X}_0). \tag{22}$$

We then utilize the fundamental solutions (kernels) of the image system for the regularized Stokes equations with a point force and torque applied to the fluid, and obtain the linear fluid velocity at an arbitrary point $\mathbf{x}$, vanishing at the wall, as follows:

$$\mathbf{u}(\mathbf{x}) = \mathbf{u}_s^{im}(\mathbf{x}) + \mathbf{u}_r^{im}(\mathbf{x}), \tag{23}$$

where

$$\mu\mathbf{u}_s^{im}(\mathbf{x}) = \mathcal{S}[\mathbf{f}_0] - \mathcal{S}^{im}[\mathbf{f}_0] + h^2\mathcal{P}[\mathbf{b}] + 2h\mathcal{D}[\mathbf{e}_3, \mathbf{b}] - 2h(\mathcal{R}_\psi[\mathbf{m}] - \mathcal{R}_\phi[\mathbf{m}]), \tag{24}$$

$$\begin{aligned}\mu\mathbf{u}_r^{im}(\mathbf{x}) = {} & \frac{1}{2}\mathcal{R}_\psi[\mathbf{n}_0] - \frac{1}{2}\mathcal{R}_\psi^{im}[\mathbf{n}_0] \\ & - (\mathcal{D}[\mathbf{p}, \mathbf{e}_3] + \mathcal{D}[\mathbf{e}_3, \mathbf{p}] + h\mathcal{P}[\mathbf{p}]) \\ & + (\mathcal{R}_\psi[\mathbf{q}] - \mathcal{R}_\phi[\mathbf{q}]) \\ & + h(\mathcal{J}_\psi[\mathbf{n}_0, \mathbf{e}_3] - \mathcal{J}_\phi[\mathbf{n}_0, \mathbf{e}_3]) - \frac{h^2}{2}\mathcal{Q}[\mathbf{n}_0],\end{aligned} \tag{25}$$

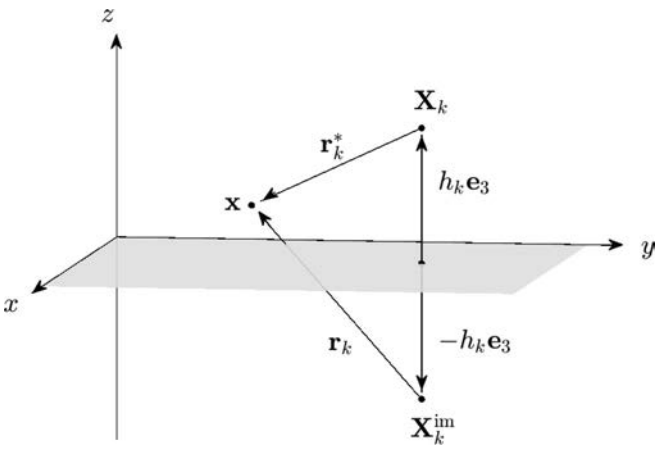

FIG. 2. Schematic geometry with the wall at $z = 0$. Velocity is evaluated at $\mathbf{x}$ with the point force and torque centered at $\mathbf{X}_k$. The image point $\mathbf{X}_k^{\text{im}}$ is introduced by the relation $\mathbf{X}_k = \mathbf{X}_k^{\text{im}} + 2h_k\mathbf{e}_3$.

where h is the distance from the wall to the point $\mathbf{X}_0$, $\mathbf{e}_3 = (0, 0, 1)$, $\mathbf{b} = 2(\mathbf{f}_0 \cdot \mathbf{e}_3)\mathbf{e}_3 - \mathbf{f}_0$, $\mathbf{m} = \mathbf{f}_0 \times \mathbf{e}_3$, $\mathbf{p} = \mathbf{n}_0 \times \mathbf{e}_3$, and $\mathbf{q} = \mathbf{n}_0 - (\mathbf{n}_0 \cdot \mathbf{e}_3)\mathbf{e}_3$. Here $\mathcal{S}$ is the regularized stokeslet, $\mathcal{P}$ is the regularized potential dipole, $\mathcal{D}$ is the regularized stokeslet doublet, $\mathcal{R}$ is the regularized rotlet, $\mathcal{J}$ is the regularized rotlet doublet, and $\mathcal{Q}$ is the regularized quadrupole. The rotlet $\mathcal{R}_\phi$ is regularized using the blob function

$$\phi_\delta(\mathbf{r}) = \frac{3\delta^2}{4\pi(|\mathbf{r}|^2 + \delta^2)^{5/2}}, \tag{26}$$

and the other kernels are regularized using ψ_δ in Eq. (12). In what follows, the angular fluid velocity at the point $\mathbf{x}$ can be obtained by

$$\mathbf{w}(\mathbf{x}) = \tfrac{1}{2}\nabla \times \mathbf{u}_s^{\text{im}} + \tfrac{1}{2}\nabla \times \mathbf{u}_r^{\text{im}} \equiv \mathbf{w}_s^{\text{im}} + \mathbf{w}_r^{\text{im}}. \tag{27}$$

We leave out here and describe in the Appendix the explicit forms of fundamental solutions and the detailed derivations of the linear and angular velocities in the image system; instead, we here introduce the computational recipe to compute the solutions. For numerical computations, we discretize the immersed boundary (flagellum and cell body) by letting $\mathbf{X}_k$, $k = 1,...,N_b$, be the discretized material points, where N_b is the number of points, and letting $\mathbf{f}_k$ and $\mathbf{n}_k$ be corresponding point forces and torques applied at the boundary point $\mathbf{X}_k$. For the notational simplicity, we substitute $\mathbf{f}_k$ and $\mathbf{n}_k$ for the point forces and torques, $-\mathbf{f}_k\Delta s$ and $-\mathbf{n}_k\Delta s$, respectively, where Δs is the mesh width of the flagellum. Then the external fluid force $\mathbf{g}$ in the regularized Stokes equations (3) can be written as

$$\mathbf{g} = \sum_{k=1}^{N_b} \mathbf{f}_k \psi_\delta(\mathbf{x} - \mathbf{X}_k) + \frac{1}{2}\nabla \times \sum_{k=1}^{N_b} \mathbf{n}_k \psi_\delta(\mathbf{x} - \mathbf{X}_k). \tag{28}$$

In the image system, we introduce an image point $\mathbf{X}_k^{\text{im}} = (x, y, -h_k)$ of $\mathbf{X}_k = (x, y, h_k)$, where h_k is the distance from the wall ($h_k > 0$), and define $\mathbf{r}_k^* = \mathbf{x} - \mathbf{X}_k$, $\mathbf{r}_k = \mathbf{x} - \mathbf{X}_k^{\text{im}}$, $r_k^* = |\mathbf{x} - \mathbf{X}_k|$, and $r_k = |\mathbf{x} - \mathbf{X}_k^{\text{im}}|$, where $\mathbf{x}$ is any point in space. See Fig. 2 for the geometric diagram. Note that $\mathbf{X}_k = \mathbf{X}_k^{\text{im}} + 2h_k\mathbf{e}_3$ and that $r_k^* = r_k$ when $\mathbf{x}$ is on the wall. Then the linear fluid velocity at any point $\mathbf{x}$ in the image system can be computed by

$$\mu\mathbf{u}(\mathbf{x}) = \mu\mathbf{u}_s^{\text{im}}(\mathbf{x}) + \mu\mathbf{u}_r^{\text{im}}(\mathbf{x}), \tag{29}$$

where $\mathbf{u}_s^{\text{im}}(\mathbf{x})$ is the velocity of the image system of the regularized stokeslet:

$$\begin{aligned}\mu\mathbf{u}_s^{\text{im}}(\mathbf{x}) = \sum_{k=1}^{N_b} \Bigg(& \{\mathbf{f}_k H_1(r_k^*) + (\mathbf{f}_k \cdot \mathbf{r}_k^*)\mathbf{r}_k^* H_2(r_k^*)\} - \{\mathbf{f}_k H_1(r_k) + (\mathbf{f}_k \cdot \mathbf{r}_k)\mathbf{r}_k H_2(r_k)\} + h_k^2\{-\mathbf{b}_k D_1^\phi(r_k) - (\mathbf{b}_k \cdot \mathbf{r}_k)\mathbf{r}_k D_2^\phi(r_k)\} \\ & + 2h_k\Big\{(\mathbf{b}_k \cdot \mathbf{e}_3)\mathbf{r}_k H_2(r_k) + (\mathbf{r}_k \cdot \mathbf{e}_3)\mathbf{b}_k H_2(r_k) + (\mathbf{b}_k \cdot \mathbf{r}_k)\mathbf{e}_3[H_3(r_k) - H_2(r_k)] \\ & + (\mathbf{r}_k \cdot \mathbf{e}_3)(\mathbf{b}_k \cdot \mathbf{r}_k)\mathbf{r}_k \frac{D_2^\phi(r_k)}{2}\Big\} + 2h_k H_3(r_k)(\mathbf{m}_k \times \mathbf{r}_k)\Bigg),\end{aligned}$$

and $\mathbf{u}_r^{\text{im}}(\mathbf{x})$ is the velocity of the image system of the regularized rotlet:

$$\begin{aligned}\mu\mathbf{u}_r^{\text{im}}(\mathbf{x}) = \sum_{k=1}^{N_b} \Bigg(& \frac{1}{2}Q(r_k^*)(\mathbf{n}_k \times \mathbf{r}_k^*) - \frac{1}{2}Q(r_k)(\mathbf{n}_k \times \mathbf{r}_k) + h_k\big[\mathbf{p}_k D_1^\phi(r_k) + (\mathbf{p}_k \cdot \mathbf{r}_k)\mathbf{r}_k D_2^\phi(r_k)\big] \\ & - \big\{[(\mathbf{p}_k \cdot \mathbf{r}_k)\mathbf{e}_3 + (\mathbf{e}_3 \cdot \mathbf{r}_k)\mathbf{p}_k]H_3(r_k) + (\mathbf{e}_3 \cdot \mathbf{r}_k)(\mathbf{p}_k \cdot \mathbf{r}_k)\mathbf{r}_k D_2^\phi\big\} \\ & - h_k[\mathbf{p}_k H_3(r_k) + (\mathbf{r}_k \cdot \mathbf{e}_3)(\mathbf{n}_k \times \mathbf{r}_k)H_4(r_k)] - H_3(r_k)(\mathbf{q}_k \times \mathbf{r}_k) + h_k^2 H_4(r_k)(\mathbf{n}_k \times \mathbf{r}_k)\Bigg),\end{aligned}$$

where the constant vectors are defined as $\mathbf{b}_k = 2(\mathbf{f}_k \cdot \mathbf{e}_3)\mathbf{e}_3 - \mathbf{f}_k$, $\mathbf{m}_k = \mathbf{f}_k \times \mathbf{e}_3$, $\mathbf{p}_k = \mathbf{n}_k \times \mathbf{e}_3$, and $\mathbf{q}_k = \mathbf{n}_k - (\mathbf{n}_k \cdot \mathbf{e}_3)\mathbf{e}_3$. The functions used here shall be summarized below.

The previous models [29,30] utilize only the linear velocity for the no-slip boundary wall given in Eq. (29). However, our model additionally requires the angular velocity to rotate the orthonormal triad $\{\mathbf{D}_k^1, \mathbf{D}_k^2, \mathbf{D}_k^3\}$ along the flagellum through Eq. (8). (For the derivation of the angular velocity in a free space, see Refs. [25,34].) The angular velocity obtained by taking curl on the linear velocity $\mathbf{u}(\mathbf{x})$ has the following formula:

$$\mu\mathbf{w}(\mathbf{x}) = \mu\mathbf{w}_s^{\text{im}}(\mathbf{x}) + \mu\mathbf{w}_r^{\text{im}}(\mathbf{x}), \tag{30}$$

where the angular velocity $\mathbf{w}_s^{\text{im}}(\mathbf{x})$ of the regularized image system for Stokelet is

$$\mu\mathbf{w}_s^{\text{im}}(\mathbf{x}) = \frac{1}{2}\nabla\times\mu\mathbf{u}_s^{\text{im}}(\mathbf{x}) = \sum_{k=1}^{N_b}\Big(\frac{1}{2}Q(r_k^*)(\mathbf{f}_k\times\mathbf{r}_k^*) - \frac{1}{2}Q(r_k)(\mathbf{f}_k\times\mathbf{r}_k) + h_k^2H_4(r_k)(\mathbf{b}_k\times\mathbf{r}_k)$$
$$+ h_k\big[D_2^\phi(r_k) - H_4(r_k)\big](\mathbf{b}_k\cdot\mathbf{r}_k)(\mathbf{e}_3\times\mathbf{r}_3) + h_kQ(r_k)\mathbf{m}_k + h_k\big\{\big[r_k^2H_4(r_k) + 2H_3(r_k)\big]\mathbf{m}_k - H_4(r_k)(\mathbf{m}_k\cdot\mathbf{r}_k)\mathbf{r}_k\big\}\Big),$$

and the angular velocity $\mathbf{w}_r^{\text{im}}(\mathbf{x})$ of the regularized image system for rotlet is

$$\mu\mathbf{w}_r^{\text{im}}(\mathbf{x}) = \frac{1}{2}\nabla\times\mu\mathbf{u}_r^{\text{im}}(\mathbf{x}) = \sum_{k=1}^{N_b}\Big(-\frac{1}{4}D_1^\psi(r_k^*)\mathbf{n}_k - \frac{1}{4}D_2^\psi(r_k^*)(\mathbf{n}_k\cdot\mathbf{r}_k^*)\mathbf{r}_k^* + \frac{1}{4}D_1^\psi(r_k)\mathbf{n}_k + \frac{1}{4}D_2^\psi(r_k)(\mathbf{n}_k\cdot\mathbf{r}_k)\mathbf{r}_k$$
$$+ \frac{1}{2}\big[H_4(r_k) - D_2^\phi(r_k)\big]\big[(\mathbf{r}_k\cdot\mathbf{e}_3)(\mathbf{p}_k\times\mathbf{r}_k) + (\mathbf{r}_k\cdot\mathbf{p}_k)(\mathbf{e}_3\times\mathbf{r}_k)\big]$$
$$- h_kH_4(r_k)(\mathbf{p}_k\times\mathbf{r}_k) - \frac{1}{2}\big[r_k^2H_4(r_k) + 2H_3(r_k)\big]\mathbf{q}_k + \frac{1}{2}H_4(r_k)(\mathbf{r}_k\cdot\mathbf{q}_k)\mathbf{r}_k$$
$$- \frac{h_k}{2}\big\{\big[r_k^2H_5(r_k) + 3H_4(r_k)\big](\mathbf{r}_k\cdot\mathbf{e}_3)\mathbf{n}_k - H_4(r_k)[(\mathbf{n}_k\cdot\mathbf{e}_3)\mathbf{r}_k + \mathbf{p}_k\times\mathbf{r}_k] - H_5(r_k)(\mathbf{r}_k\cdot\mathbf{e}_3)(\mathbf{r}_k\cdot\mathbf{n}_k)\mathbf{r}_k\big\}$$
$$+ \frac{h_k^2}{2}\big\{\big[2H_4(r_k) + r_k^2H_5(r_k)\big]\mathbf{n}_k - H_5(r_k)(\mathbf{r}_k\cdot\mathbf{n}_k)\mathbf{r}_k\big\}\Big).$$

We now provide the definition of functions used in the above formula. Let G_ψ and B_ψ be the regularized Green's function and biharmonic function, respectively, satisfying $\Delta G_\psi(\mathbf{r}) = \psi_\delta(\mathbf{r})$ and $\Delta B_\psi(\mathbf{r}) = G_\psi(\mathbf{r})$. Then the functions H_1, H_2, Q, D_1^ψ, and D_2^ψ are defined as

$$H_1(r) = \frac{B_\psi'}{r} - G_\psi = \frac{2\delta^2 + r^2}{8\pi(\delta^2 + r^2)^{3/2}}, \tag{31}$$

$$H_2(r) = \frac{rB_\psi'' - B_\psi'}{r^3} = \frac{1}{8\pi(\delta^2 + r^2)^{3/2}}, \tag{32}$$

$$Q(r) = \frac{G_\psi'}{r} = \frac{5\delta^2 + 2r^2}{8\pi(\delta^2 + r^2)^{5/2}}, \tag{33}$$

$$D_1^\psi(r) = \frac{G_\psi'}{r} - \psi_\delta = \frac{-10\delta^4 + 7r^2\delta^2 + 2r^4}{8\pi(\delta^2 + r^2)^{7/2}}, \tag{34}$$

$$D_2^\psi(r) = \frac{rG_\psi'' - G_\psi'}{r^3} = \frac{-21\delta^2 - 6r^2}{8\pi(\delta^2 + r^2)^{7/2}}. \tag{35}$$

For a more slowly decaying blob function ϕ_δ in Eq. (26), we can find the regularized Green's function G_δ satisfying $\Delta G_\phi(\mathbf{r}) = \phi_\delta(\mathbf{r})$ and the regularized biharmonic function B_ϕ satisfying $\Delta B_\phi(\mathbf{r}) = G_\phi(\mathbf{r})$. Then the dipole functions D_1^ϕ and D_2^ϕ and H_3, H_4, and H_5 are defined as

$$D_1^\phi(r) = \frac{G_\phi'}{r} - \phi_\delta = \frac{-2\delta^2 + r^2}{4\pi(\delta^2 + r^2)^{5/2}}, \tag{36}$$

$$D_2^\phi(r) = \frac{rG_\phi'' - G_\phi'}{r^3} = \frac{-3}{4\pi(\delta^2 + r^2)^{5/2}}, \tag{37}$$

$$H_3(r) = \frac{G_\phi'}{r} - \frac{G_\psi'}{r} = \frac{H_1'}{r} + H_2 = \frac{-3\delta^2}{8\pi(\delta^2 + r^2)^{5/2}}, \tag{38}$$

$$H_4(r) = \frac{(D_1^\phi)'}{2r} - \frac{D_2^\phi}{2} = \frac{(D_1^\phi)'}{2r} - \frac{H_2'}{r} = \frac{15\delta^2}{8\pi(\delta^2 + r^2)^{7/2}}, \tag{39}$$

$$H_5(r) = \frac{H_4'}{r} = \frac{-105\delta^2}{8\pi(r^2 + \delta^2)^{9/2}}. \tag{40}$$

IV. RESULTS AND DISCUSSION

In this section, we investigate the hydrodynamics of a single-flagellated bacterium when it is placed near a planar wall $z = 0$. See Fig. 1 for a schematic diagram of our computational model in which $h(t)$ is the distance of the center of mass of the cell body from the wall, and $\theta(t)$ is the inclination angle of the major axis of the cell body from $z = 0$ at time t. Our model swimmer initially lies in parallel to the wall with $\theta(0) = 0$. However, the initial distance $h(0)$ varies with

TABLE I. Computational and physical parameters.

Parameters	Symbol	Value
Fluid viscosity	μ	10^{-6} g/(μm s)
Regularization parameter	δ	$3\Delta s$
Time step	Δt	1.0×10^{-8} s
Mesh width for flagellum	Δs	0.04 μm
Helical radius of filament	r_0	0.1989 μm
Helical pitch of filament	p_0	1.25 μm
Linear length of filament	L	3.75 μm
Intrinsic curvature of filament	κ	2.5133 μm^{-1}
Intrinsic twist of filament	Ω_3	2.5133 μm^{-1}
Bending modulus of filament	a_1, a_2	0.04 gμm^3/s^2
Twist modulus of filament	a_3	0.04 gμm^3/s^2
Shear modulus	b_1, b_2	2.0 gμm/s^2
Stretch modulus	b_3	2.0 gμm/s^2
Rotation rate of motor	ω	500 Hz
Spherical cell body diameter	$2A$	1.0 μm
Cell body density	m	10^{-12} g/μm^2

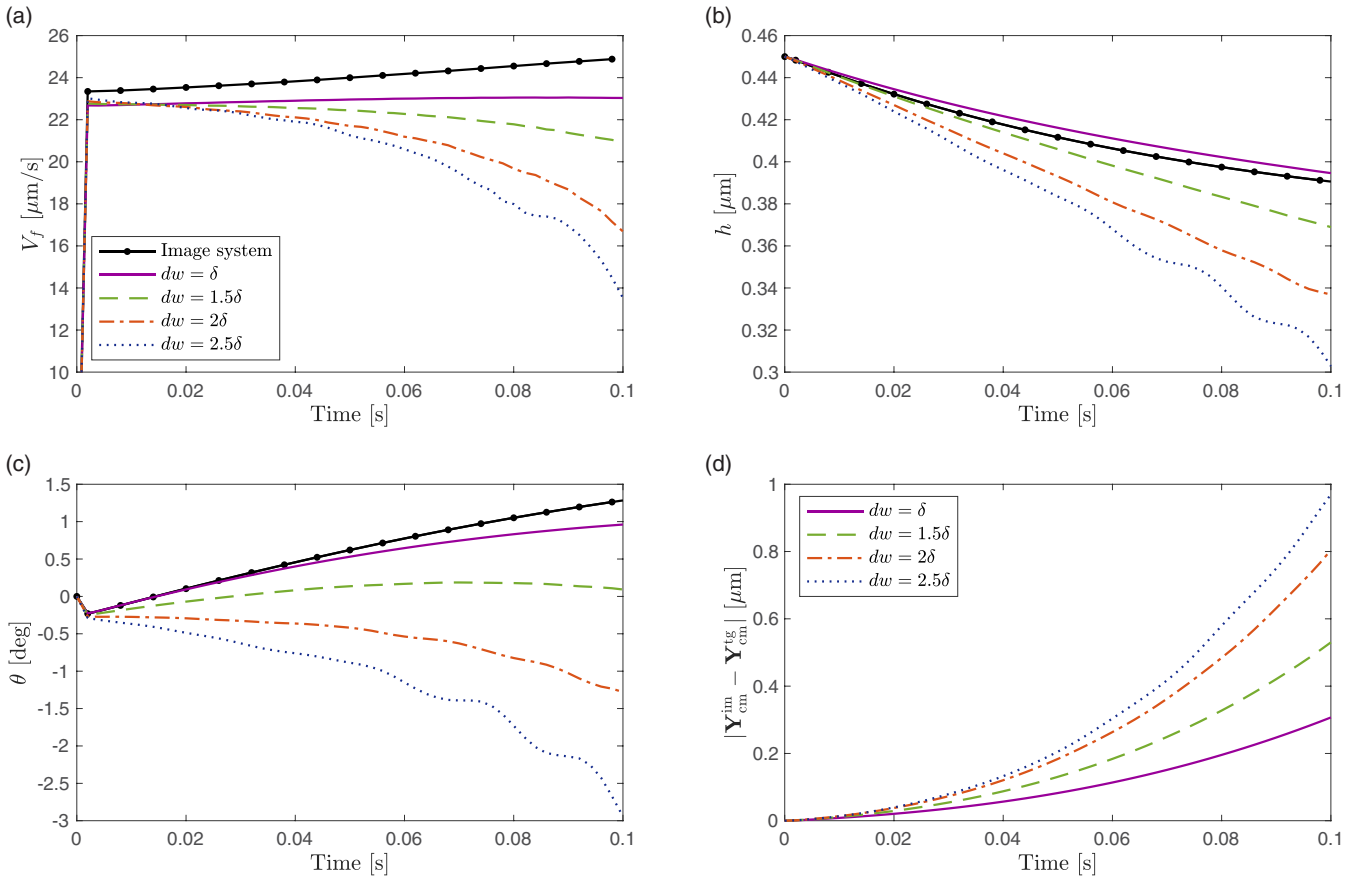

FIG. 3. Comparisons between the image system method (solid lines with circles) and the target point method when $dw = 1.0\,\delta$ (solid), $1.5\,\delta$ (dashed), $2.0\,\delta$ (dash-dotted), and $2.5\,\delta$ (dotted) in terms of the forward swimming speed $V_f(t)$ (a), distance from the wall $h(t)$ (b), inclination angle $\theta(t)$ (c), and distance from the center of mass of the cell body in the image system method to those of the target point method (d).

different simulations. Table I shows the computational and physical parameters used in this work.

A. Comparison of the image system method with target point method

We first verify the efficiency of the image system method by comparing it with the target point method. In the target point method, we impose the no-slip condition on the plane $z = 0$ by laying out an array of target points. Let $\mathbf{W}(r, s)$ be the target points tethered on the plane $z = 0$ and $\mathbf{X}_w(r, s, t)$ be the corresponding moving boundary points. A no-slip condition on the wall is imposed by applying to the moving boundary $\mathbf{X}_w(r, s, t)$ the following force:

$$\mathbf{F}_w(r, s, t) = c_0[\mathbf{W}(r, s) - \mathbf{X}_w(r, s, t)], \tag{41}$$

where c_0 is a large constant and $\mathbf{X}_w(r, s, t)$ moves at the local fluid velocity. This provides a feedback mechanism for computing the boundary force needed to enforce the moving boundary points to stay close to the target points. For comparisons, we choose a square with a side length of 7.2 μm on $z = 0$, and distribute $(N + 1)^2$ target points uniformly on the square. The mesh size of the square domain in each direction is chosen as $N = 24, 30, 40,$ and 60, and thus the corresponding mesh widths are $dw = 2.5\,\delta$ μm, $2.0\,\delta$ μm, $1.5\,\delta$ μm, and $1.0\,\delta$ μm, respectively, where δ is the regularization parameter used in Eq. (12). The model bacterium, which has a spherical cell body with radius 0.3 μm, and a helical flagellum with radius $r_0 = 0.1194$ μm, pitch $p_0 = 0.75$ μm, and linear length $L = 2.25$ μm, is placed in parallel to the wall with initial distance $h(0) = 0.45$ μm. The motor rotates CCW at a rate of 500 Hz. The time step used for this test is $\Delta t = 1.25 \times 10^{-8}$ s, and the other parameters are the same as in Table I.

Figure 3 compares the simulation results obtained by the regularized image system method (solid lines with circles) and by the target point method with four different mesh widths $dw = 1.0\,\delta$ (solid lines), $1.5\,\delta$ (dashed lines), $2.0\,\delta$ (dash-dotted lines), and $2.5\,\delta$ (dotted lines). We compare the forward swimming speed $V_f(t)$ [Fig. 3(a)], the distance from the wall $h(t)$ [Fig. 3(b)], the inclination angle $\theta(t)$ [Fig. 3(c)], and the distance between the cell centers of $\mathbf{Y}_{\rm cm}^{\rm tg}$ in the target point method and $\mathbf{Y}_{\rm cm}^{\rm im}$ in the image system method [Fig. 3(d)]. The forward-directional swimming speed is defined as $V_f(t) = -\mathbf{V}_{\rm cm}(t) \cdot \mathbf{E}_3(t)$. Figure 3 shows that as we increase the number of target points and thus refine the mesh of the square, the difference between the results of the image system method and the target point method gets smaller.

The main reason for the discrepancy between the image system and target point methods is the following. While the

TABLE II. Computational times.

Method	Mesh width (dw)	Grid size (N)	Wall time (s)
Target point method	$2.5\,\delta$	25^2	26.6255
	$2.0\,\delta$	31^2	44.3190
	$1.5\,\delta$	41^2	87.9813
	$1.0\,\delta$	61^2	356.0195
Image system method	–	–	18.5712

no-slip boundary condition is exactly prescribed on the whole plane $z = 0$ in the former method, it is only approximately true on the part (square) of the plane $z = 0$ in the latter one. Note that the size of the target domain on the wall here is large enough to resolve the motion of the model bacterium, and hence a larger target domain does not significantly improve the discrepancy. However, the error of the approximated no-slip condition would be decreased by increasing the constant c_0 in Eq. (41) or by decreasing the mesh width dw as shown in Fig. 3. All these cases require us either to decrease the time step Δt due to the stability condition or to increase the number of the target points, which would make the computation for a realistic bacterial model impossible. Since, instead of adding more target points, the method of image system adds some additional regularized solutions at the given immersed boundary points as explained in the previous section, it is computationally much more efficient to make a no-slip planar wall. Table II shows the computation times from the two methods. In both methods, we used OpenMP parallelization with 16 nodes, and the wall time is measured for 20 000 iterations. For the comparable case of $dw = \delta$, the computational time of the target point method takes 19 times more than that of the image system method for the same number of iterations.

B. Stable circular motion of a model organism with a spherical cell body

It has been experimentally and numerically observed that flagellated bacteria change their trajectories from straight to circular near a solid surface [11,12,16–18,20,21]. A hydrodynamic attraction toward the wall occurs due to the image singularities located on the other side of the surface [35]; however, when the bacteria are too close to the wall, the wall repels the bacteria to give a stable height h^*. This proximity may enhance the chance of the cell's adhesion to the surface, which may facilitate biofilm formation [13–15]. In the absence of solid surfaces, the CCW rotation of the left-handed flagellum driven by the CCW rotation of the motor generates the thrust that is opposed by the viscous drag on the cell and leads to a straight forward run. At the same time, the motor rotation exerts a countertorque on the cell body to balance the torque which induces CW rotation of the cell body. Near a solid surface, the balance between the opposite torques on the cell body and on the rotating flagellum and its hydrodynamic interaction with the solid surface deviates the swimming path from a straight line to a CW circle when viewed from above the surface [20].

In order to explore the characteristic swimming patterns of bacteria near the surface $z = 0$, We first consider a bacterium which is composed of a spherical cell body with diameter $2A = 1.0\ \mu$m and a left-handed helical flagellum with helical radius $r_0 = 0.1989\ \mu$m, helical pitch $p_0 = 1.25\ \mu$m, and number of wavelength $N_\lambda = 3$. This model organism is initially positioned in parallel to the wall with various initial heights $h(0)$ from 0.55 to 1.0 μm. The flagellar motor turns CCW at the rate of $\omega = 500$ Hz at all times. Figure 4 shows time evolution of a bacterial movement when the initial height is set as $h(0) = 1.0\ \mu$m; see Movie 1 in the Supplemental Material [36]. Two aspects of the motion are displayed: one viewed from the side [Fig. 4(a)] and the other viewed toward the wall from above [Fig. 4(b)]. It is shown that the model organism swims toward the wall to eventually stay at almost a constant height and to draw a CW circular trajectory with an approximately constant radius. Note that the cell body is observed to rotate CW at the rate of approximately 41 Hz, and that a cell with a right-handed flagellum turning its motor CW swims in a CCW circle (data not shown).

Figure 5 shows that there is a limiting stable circular motion of the bacterium near a surface independent of the initial height $h(0)$ as long as it is within a certain range. As the initial height $h(0)$ varies from 0.55 to 1.0 μm, the bacterium goes to a stable state of the swimming pattern in which height $h(t)$ [Fig. 5(a)], inclination angle $\theta(t)$ [Fig. 5(b)], forward swimming speed $V_f(t)$ [Fig. 5(c)], and radius $R(t)$ of the circular trajectory [Fig. 5(d)] converge approximately to $h^* = 0.5529\ \mu$m, 2.99°, $50.32\ \mu$m/s, and $7.46\ \mu$m, respectively. The radius of curvature $R(t)$ of the circular trajectory is defined as the reciprocal of the local curvature of a circular trajectory at time t. Note that the positive inclination angle θ in Fig. 5(b)] indicates that the cell body points away from the wall, which is needed to balance the attractive effect of near-wall swimming bacteria and the lift force on the cell body [21]. Note also that if bacteria are placed far enough away from the wall, they stay away from the trapping zone, which we define by the region near the wall in which bacteria swim without escaping.

We now investigate the dependence of the swimming patterns of bacteria near a wall on various physical and geometrical parameters of our bacterium model. We first vary the motor frequency, ω, from 300 to 700 Hz to compare height $h(t)$ (a), inclination angle $\theta(t)$ (b), forward swimming speed $V_f(t)$ (c), and radius $R(t)$ of the circular trajectory (d); see Fig. 6. We fix the initial height at $h(0) = 0.6\ \mu$m; however, we have found that the limiting values in the stable state are independent of the initial height $h(0)$ (not shown here). Figure 6 demonstrates that the cell reaches a stable motion with a circular trajectory; however, the limiting values of some swimming properties change depending on the rotation rate of the motor. As the motor frequency ω increases, the limiting values of $h(t)$, $\theta(t)$, and $V_f(t)$ increase as well. In particular, the limiting height and the forward swimming speed increase almost proportionally to the rotation rate. The radii $R(t)$ of circular trajectories increase during the transient time as the motor frequency increases; however, they converge to approximately the same constant radius.

Unlike the previous models of the flagellum used in Refs. [7,20,21], which is a helical rigid body rotated by imposing its dynamics (velocity or position), our flagellum model is an elastic body which rotates through the torque propagated

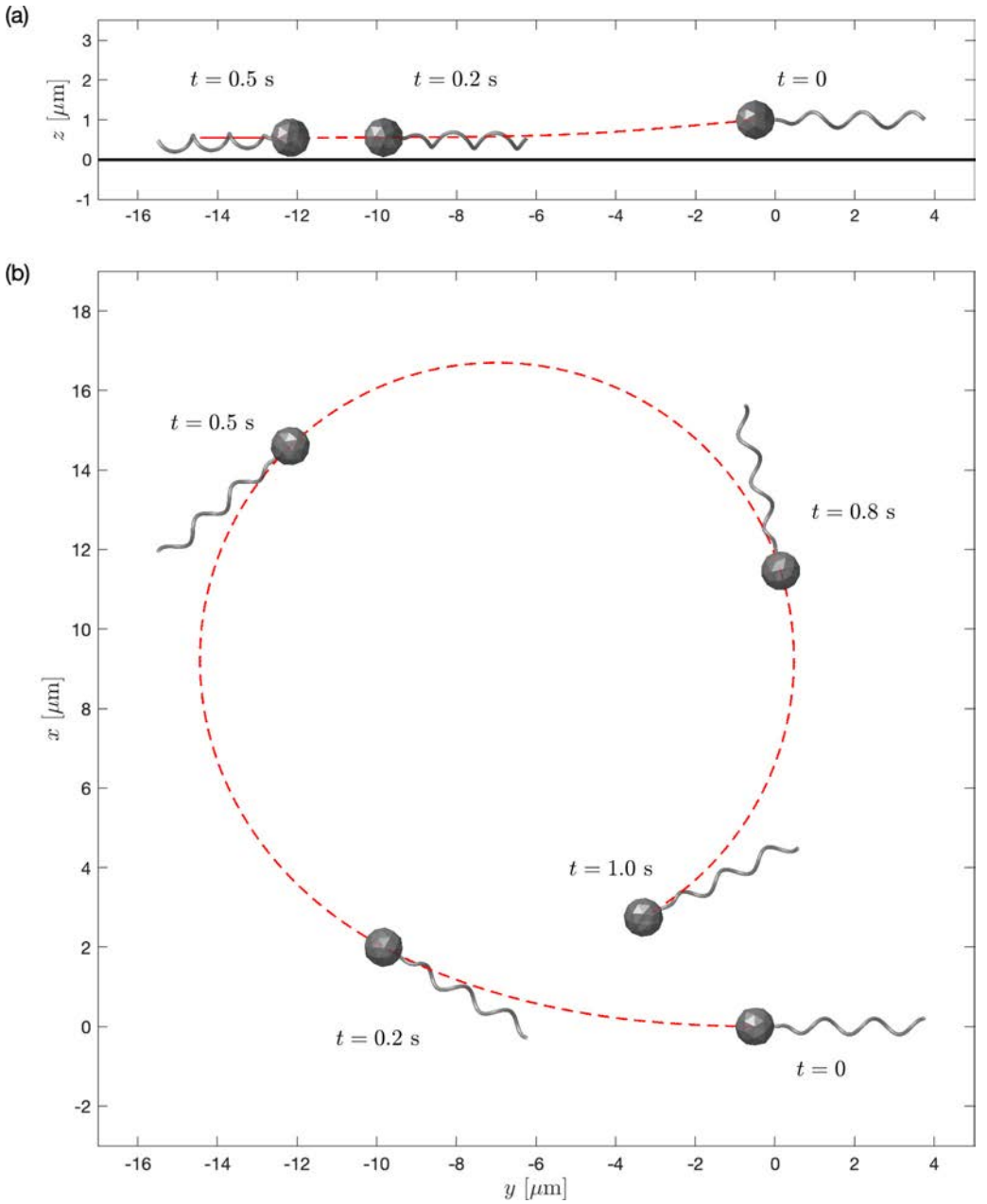

FIG. 4. Motion of a bacterium viewed from side (a) and viewed toward the wall (b). The cell, initially positioned in parallel to the wall ($z = 0$) with height $h(0) = 1.0$ μm, swims toward the wall and follows a circular trajectory.

from the rotating motor. In order to demonstrate the difference of the swimming patterns of bacteria near a wall depending on the elastic property of the flagellum, Fig. 7 shows the limiting values of steady circular trajectories resulting from the changes in the bending modulus $a_1 = a_2$ (left panels) and the twist modulus a_3 (right panels). As the bending modulus increases from 0.005 to 0.16 gμm^3/s^2, the limiting values of height h^* and the forward swimming speed V_f^* decrease, while the radius R^* of the circular trajectories increases; see Figs. 7(a)–7(c). When the twist modulus increases from 0.005 to 0.16 gμm^3/s^2, the limiting value V_f^* increases; however, h^* and R^* decrease slightly; see Figs. 7(f)–7(h).

The different elastic stiffness of the flagellum does not only affect the three limiting values, but it also induces the change of the geometrical properties of the flexible flagellum. The lower two rows of Fig. 7 depict the measured values of the helical pitch [Figs. 7(d) and 7(i)] and the helical radius [Figs. 7(e) and 7(j)] of the rotating flagellum together with those of the initial flagellum in the equilibrium state (dashed lines). As the bending modulus increases, the helical pitch increases to the equilibrium value, while the helical radius is almost fixed. The increment of the twist modulus, however, increases the helical radius up to the equilibrium value with the helical pitch being almost fixed. The bending energy comes into play when the curvature of the moving helix deviates from its intrinsic curvature, which results mostly in the change of helical pitch, whereas the twist energy is related to the intrinsic twist of flagellum and thus the helical radius. We have

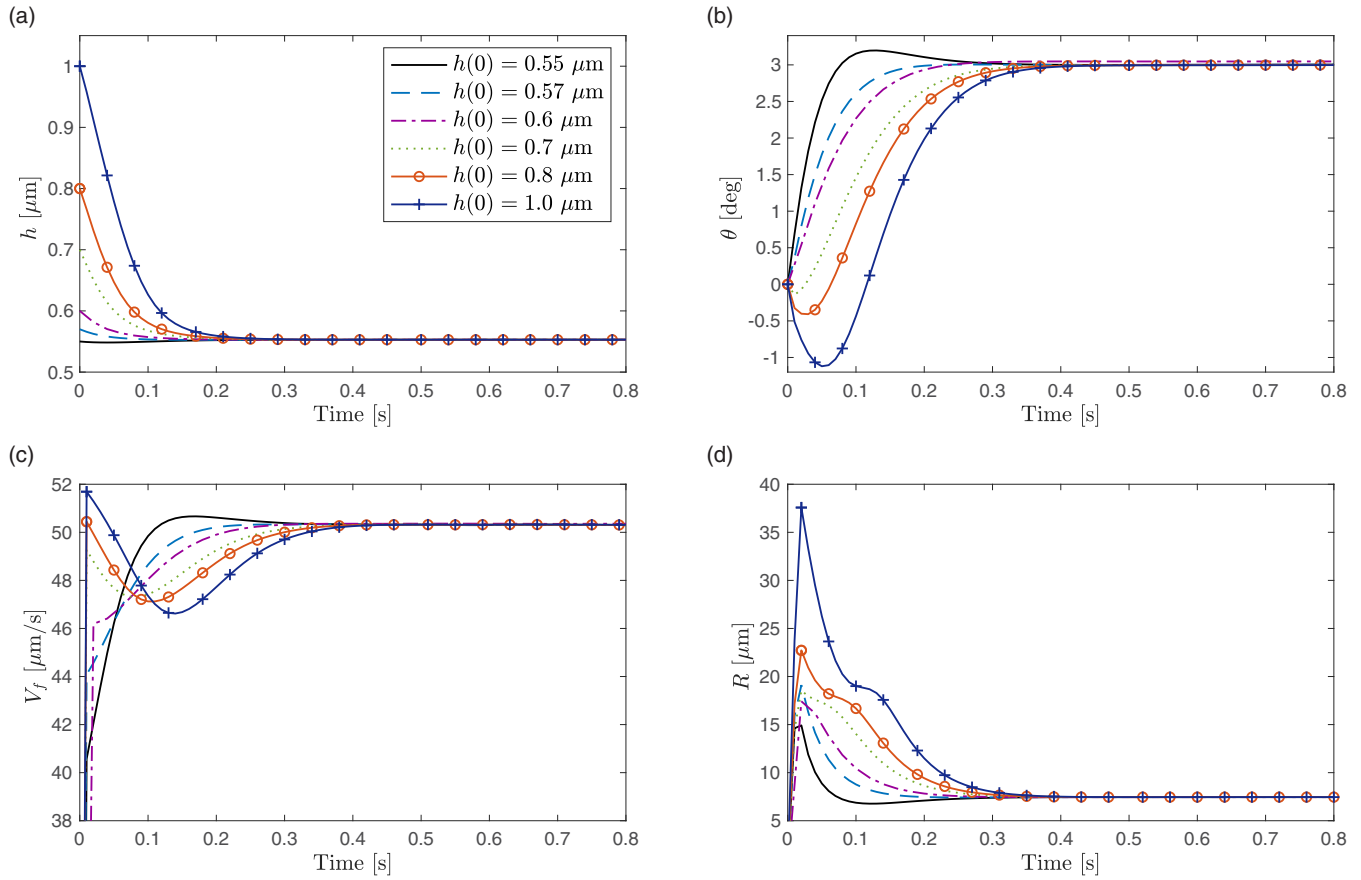

FIG. 5. Time evolution of height $h(t)$ (a), inclination angle $\theta(t)$ (b), forward swimming speed $V_f(t)$ (c), and radius $R(t)$ of a circular trajectory (d) for various initial heights $h(0)$.

found that when the two moduli increase to 0.16 gμm^3/s^2, the helical pitch and radius of the rotating flagellum deviate from its intrinsic values by as much as 0.5%.

Last, we investigate how the geometrical parameters of the bacterium model affect its swimming course near a solid surface. We vary one geometrical parameter among cell body diameter $2A$, helical radius r_0, helical pitch p_0, and number of helical turns $N_\lambda = L/p_0$ along the flagellum, while the other geometrical parameters are fixed at default values: $2A = 1.0\ \mu$m, $r_0 = 0.1989\ \mu$m, $p_0 = 1.25\ \mu$m, and $N_\lambda = 3$. The other physical parameter values are the same as in Table I, and the motor frequency is fixed at $\omega = 500$ Hz. Figure 8 shows the limiting values of steady circular swimming resulting from the changes in each of four geometrical parameters; $2A$ [Fig. 8(a)], r_0 [Fig. 8(b)], p_0 [Fig. 8(c)], and N_λ [Fig. 8(d)]. For each case of parameter change, we display the limiting values of the separation gap $h^* - A$, forward swimming speed V_f^*, and radius R^* of the circular trajectory.

Figure 8(a) demonstrates that, as the diameter $2A$ of the cell body increases, the separation gap $h^* - A$, which is the minimum distance between the surface of the cell body and the bottom wall, decreases; i.e., a bacterium which has a larger cell body swims closer to the wall. Moreover, it shows that the larger the diameter of the cell body is, the slower the bacteria swim. This is because the viscous drag increases with the size of the cell body [20], which consequently decreases the swimming speed. Although the swimming speed and the separation gap change depending on the cell body size, the radii of the circular trajectories are almost the same independent of the cell body size.

Figure 8(b) shows that as the helical radius r_0 increases, the limiting value of the separation gap $h^* - A$ increases slightly and the swimming velocity V_f^* increases largely, whereas the limiting radius R^* of the circular trajectory decreases. It has been reported that a bacterium with a flagellum with a larger helical radius swims faster but follows a smaller circular trajectory [20].

As we increase the helical pitch p_0 or the number of helical turns N_λ, the flagellar contour length also increases in either case, and the limiting values of the swimming speed V_f^* and the radius R^* of circular trajectories also increase; see Figs. 8(c) and 8(d). However, the limiting values of the separation gap $h^* - A$ are approximately the same regardless of increasing p_0 and N_λ. The simulation results in this section are qualitatively well matched with the results in Ref. [20]. Note, however, that if the contour length of the flagellum is too short, the cell may leave the trapping zone and stay away from the wall, as discussed in the next section.

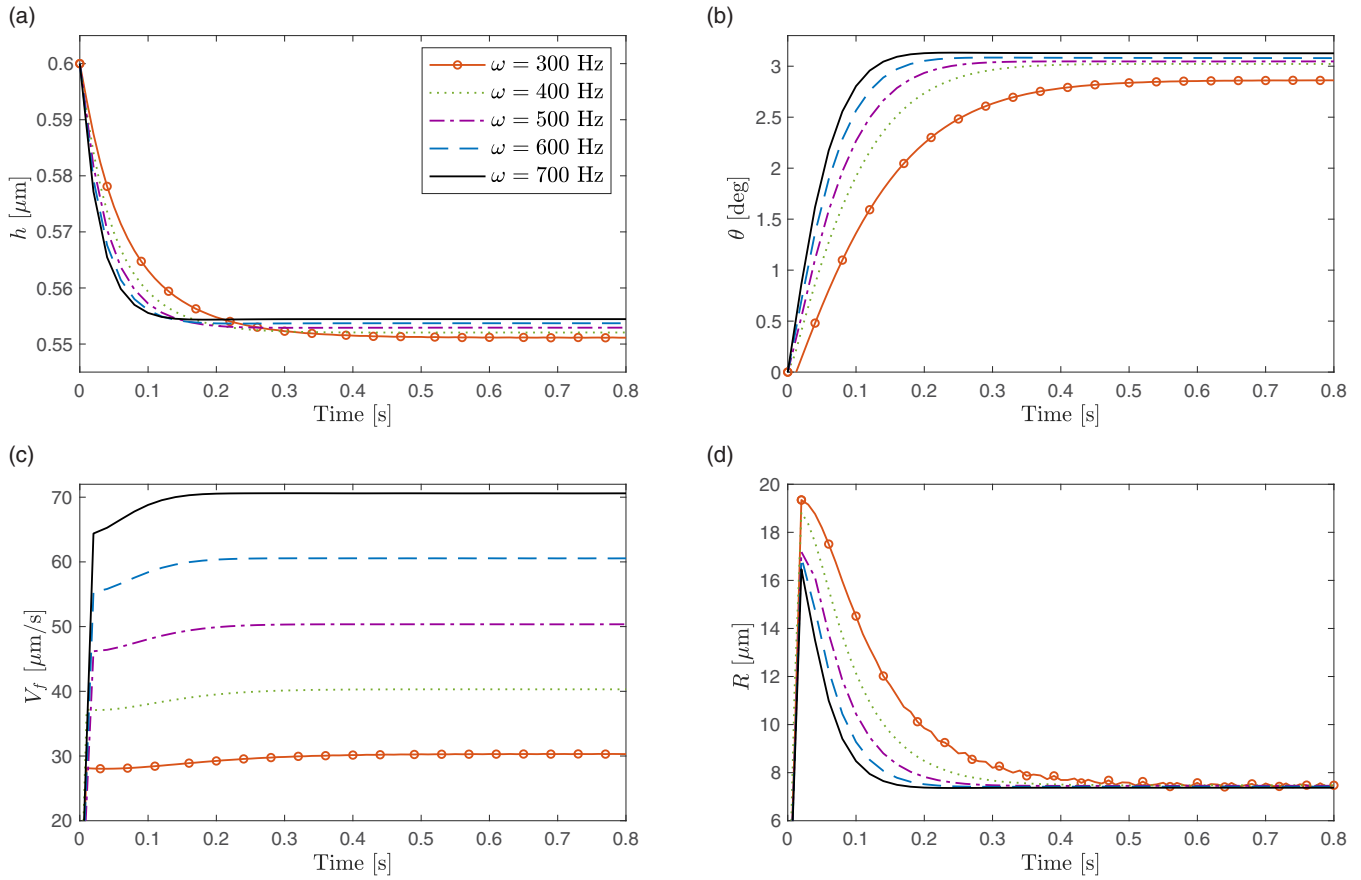

FIG. 6. Time evolution of the height $h(t)$ (a), the inclination angle $\theta(t)$ (b), the forward swimming speed $V_f(t)$ (c), and the radius $R(t)$ of the circular trajectory (d) for various motor frequencies ω from 300 to 700 Hz. There is a limiting stable swimming pattern in each case. As we increase the motor frequency, the limiting values of $h(t)$, $\theta(t)$, and $V_f(t)$ all increase. The limiting value of radius $R(t)$ is independent of the frequency ω.

C. Circular motions of a bacterium with an ellipsoidal cell body

In this section, we replace the spherical cell body by a prolate spheroid with various aspect ratios A/B, where $2A$ and $2B$ are the lengths of the major and minor axes, respectively, to investigate how the shape of the cell body alters the swimming motion of the bacterium near a solid wall. It is known that as single-flagellated cells grow, their cell bodies elongate the major axis without extending the minor axis and thus the aspect ratio A/B increases [21]. Figure 9 shows trajectories of bacteria with five different aspect ratios $A/B = 1$, 1.3, 1.4, 1.6, and 1.8, while keeping $2B = 1.0$ μm; see Movie 2 in the Supplemental Material [36]. The other parameter values are the same as in Table I. As the aspect ratio A/B of the cell body increases, the limiting radius R^* of the circular trajectory increases, illustrating that a longer cell body draws a larger circular path, which is well matched with the results in Shum *et al.* [21]. We have also found that each bacterium with a spheroidal cell body converges to a stable swimming state independent of the initial height.

Figure 10 displays the limiting values of the forward swimming speed V_f^* [Fig. 10(a)], height h^* [Fig. 10(b)], inclination angle θ^* [Fig. 10(c)], and radius R^* of the circular trajectory (d) as functions of the cell body ratio A/B. As the length A of the major axis of the cell body increases, the forward swimming speed V_f^* first increases and then decreases, attaining the maximum speed around $A/B = 1.3$. In contrast, height h^*, inclination angle θ^*, and radius R^* increase monotonically with the increasing aspect ratio. These results are also consistent with the results in the previous studies [11,21].

We can expect from these simulations that as the cell body increases further its aspect ratio, the bacterium swims in a circle with a larger radius and farther away from the wall with the cell body pointing further to the free space, and it may eventually escape from the trapping zone and swim freely without any interaction with the wall. Thus we categorize the behavior of the flagellated bacteria near a solid wall into two modes, *entrapment* and *escape*. Entrapment mode is the motion when the cell stays near the wall and swims in a circular manner, whereas escape mode is the motion when the cell swims away from the wall and becomes eventually unaffected by the wall. In order to investigate the cell's modes of motility, we consider bacteria with various flagellar lengths and aspect ratios of the cell body. We vary the length of the helical flagellum by varying the number of helical turns, N_λ, from 1.0 to 3.0, with the fixed helical pitch and radius assigned to 1.25 and 0.1989 μm, respectively. The aspect ratio of the cell body A/B is also changed from 1.2 to 1.9 with the increment of 0.1, with the minor axis being fixed at $B = 0.5$ μm. The cells are initially positioned near the wall

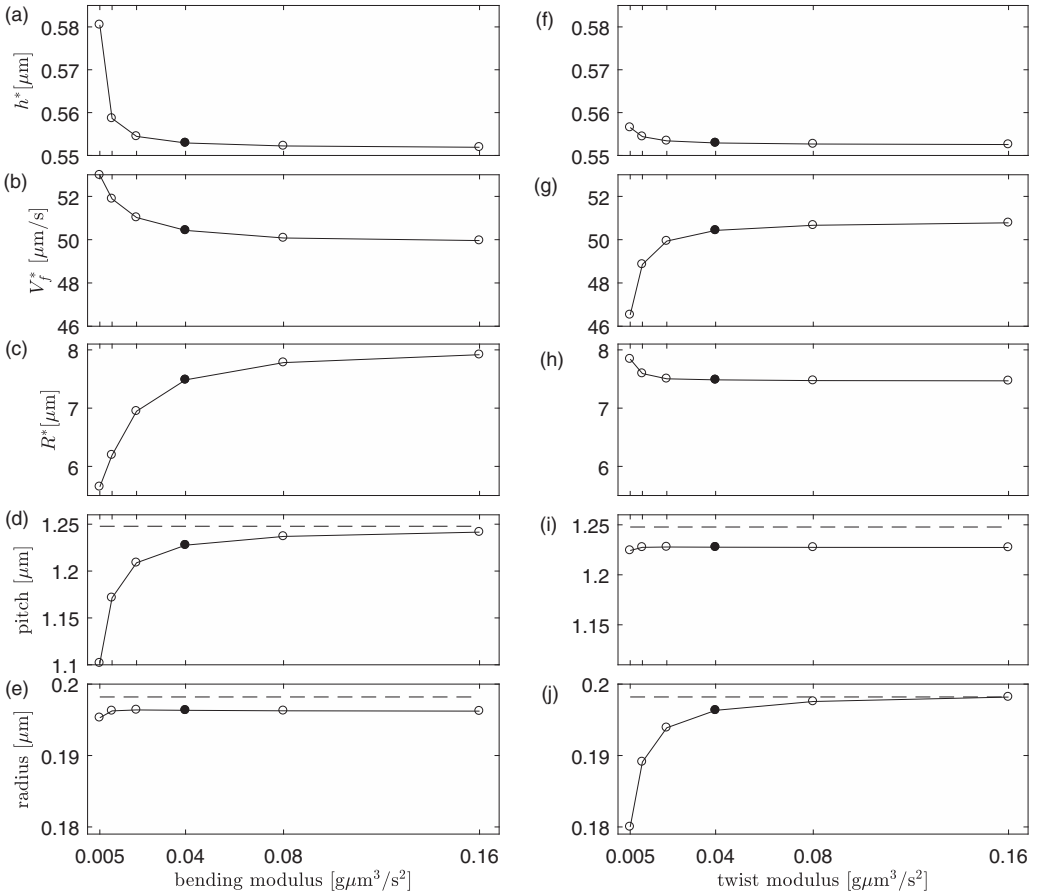

FIG. 7. Limiting values of steady circular swimming motions resulted from changes in the bending modulus $a_1 = a_2$ (left panels) and the twist modulus a_3 (right panels). For each change of the modulus, five types of limiting values are measured: the height h^* (a), (f), the forward swimming speed V_f^* (b), (g), the radius R^* of the circular trajectory (c), (h), the helical pitch (d), (i), and the helical radius (e), (j) of the rotating flagellum together with those of the initial flagellum in the equilibrium state (dashed lines). Filled circles represent the case with the default values of the elastic moduli.

at a height of $h(0) = 1.5$ μm, and the motor frequency is $\omega = 500$ Hz.

Figure 11 shows the critical values of the number of helical turns (N_λ) as the aspect ratio of the cell body changes. We find that for each aspect ratio, there exists a critical value of the number of helical turns (N_λ) that separates escaping cells from entrapped cells. The circles in blue represent the cases where the cell draws a stable circular trajectory and is entrapped near the wall, while the crosses in red represent the cases where the cell escapes and moves away from the wall. The solid line in black is an interpolated curve that separates escape zone (shaded area) from entrapment zone (white area). This curve implies that the critical number of helical turns increases almost quadratically as the cell body's aspect ratio increases. Overall, bacteria with a shorter flagellum and a longer cell body are prone to escape from the wall [21]. See Movie 3 in the Supplemental Material [36] for two modes of motility, escape and entrapment.

V. SUMMARY AND CONCLUSIONS

We have presented a comprehensive model for a swimming bacterium which is made of a cell body and a flagellum which are linked by sharing the same motor point that is embedded in the cell membrane. The cell body is a rigid body in the shape of either a sphere or a spheroid of which the dynamics is described by the penalty method. The elastic flagellum is described by the Kirchhoff rod theory as a space curve together with orthonormal triads along the rod. In our model, the rotary motor is the only driving force that results in the rotation of the flagellum that pushes the cell in motion and the counterrotation of the cell body to balance torque. The hydrodynamic interaction between the fluid and the cell is represented by the regularized Stokes formulation. In addition, the linear and angular fluid velocities in the Stokes flow are modified to account for the effect of the rigid wall using the method of an image system. In this work, the flagellum can represent a single flagellum for monotrichous bacteria or a flagellar bundle for peritrichous bacteria.

The efficiency of our model has been verified by comparing two simulation results done using the method of an image system and the target point method. We have shown that as the resolution (the number of the target points) of the planar wall increases, the numerical solution of the target point method approaches that of the image system method. However, the target point method is computationally more expensive and less efficient, while the method of an image system is naturally more accurate and efficient.

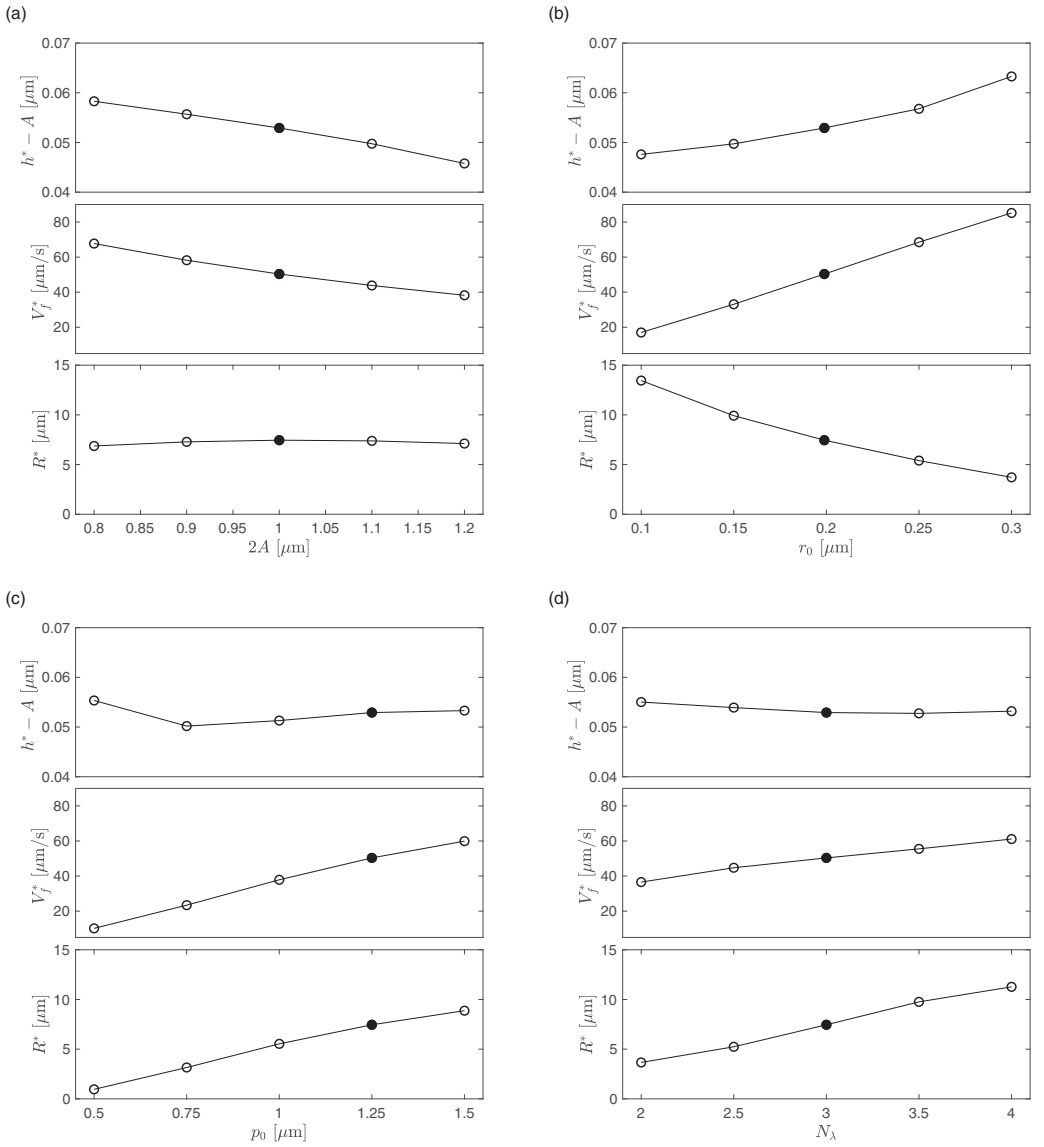

FIG. 8. Limiting values of steady circular swimming motions resulted from changes in four geometrical parameters; the diameter of the cell body $2A$ (a), the helical radius r_0 (b), the helical pitch p_0 (c), and the number of helical turns N_λ (d). For each change of the parameter, three types of limiting values are measured: the separation gap $h^* - A$ (upper panel), the forward swimming speed V_f^* (middle panel), and the radius R^* of the circular trajectory (lower panel). Simulation results with the default values are marked with filled circles.

It is known that, whereas single- and multi-flagellated bacteria approximately swim straight during the running mode in a free space, such bacteria change their swimming course from straight to circular trajectories in the presence of a solid surface nearby. Our simulations have showed that the cell swimming near a solid surface is entrapped in a region close to the surface and draws a stable circular trajectory with limiting steady values of circular radius, height from the surface, swimming speed, and inclination angle. We have also found that, whereas these limiting values are independent of the initial height of the cell, they change generally depending on the rotation rate of the motor, size of the cell body, and geometrical properties of the flagellum.

A very common shape of the cell body in flagellated bacteria is a prolate spheroid; therefore, the aspect ratio of the cell body plays a key role in determining swimming patterns. Our simulations have showed that as the cell body is elongated in the swimming direction, i.e., its aspect ratio increases, the limiting values of the height, inclination angle, and radius of the circle increase monotonically. However, there is an optimal aspect ratio for the maximal swimming speed, which is approximately obtained at $A/B = 1.3$. It is worth mentioning that this optimal condition is met when the length of the minor axis of the cell body is fixed. It may change the condition as the length of the minor axis vary, which requires a significant amount of computations.

In addition to the stable circular trajectory near a solid wall, cells can also swim away from the wall depending on the flagellar length and the aspect ratio of the cell body. Our simulations have shown that the critical number of helical turns, corresponding to the flagellar length, is quadratically proportional to the aspect ratio of the cell body. In other words, the cells can escape from the wall when the cell body is elongated in the swimming direction or when the

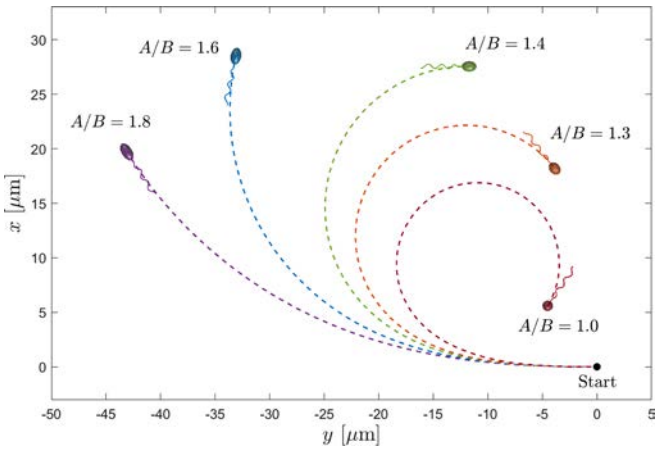

FIG. 9. Trajectories of bacteria with five different body ratios A/B. The minor axis B of the spheroidal cell body is fixed as $B = 0.5$ μm and the major axis A is varied from 0.5 to 0.9 μm. The motor frequency is set at $\omega = 500$ Hz, and all bacteria are initially placed at the same location indicated by the black dot ("Start"). The final position of cells is captured when $t = 1.0$ s. The wall is located at $z = 0$, and the trajectories are viewed toward the wall from above.

flagellar length becomes shorter, which would be considered to be mutant cells. The wild-type microorganisms might have optimal physical conditions which facilitate the migration and

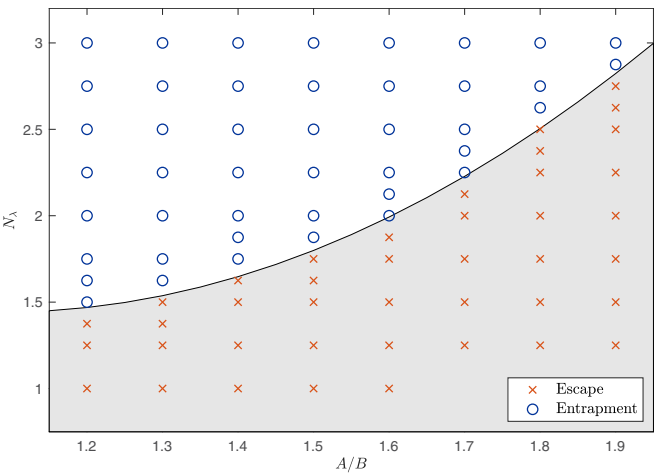

FIG. 11. Critical values of helical turns N_λ as the aspect ratio A/B of the cell body changes. The cell body ratio A/B is varied from 1.2 to 1.9 μm, while the minor axis B of the spheroidal cell body is fixed as $B = 0.5$ μm. The helical pitch and radius are fixed at 1.25 μm and 0.1989 μm, respectively. The motor frequency is set at $\omega = 500$ Hz, and the initial height is given at $h(0) = 1.5$ μm. The circles in blue represent the case of entrapped cells, and the crosses in red represent the case of escaping cells. The solid line in black is an interpolated curve that separates the escape zone (shaded area) from the entrapment zone (white area).

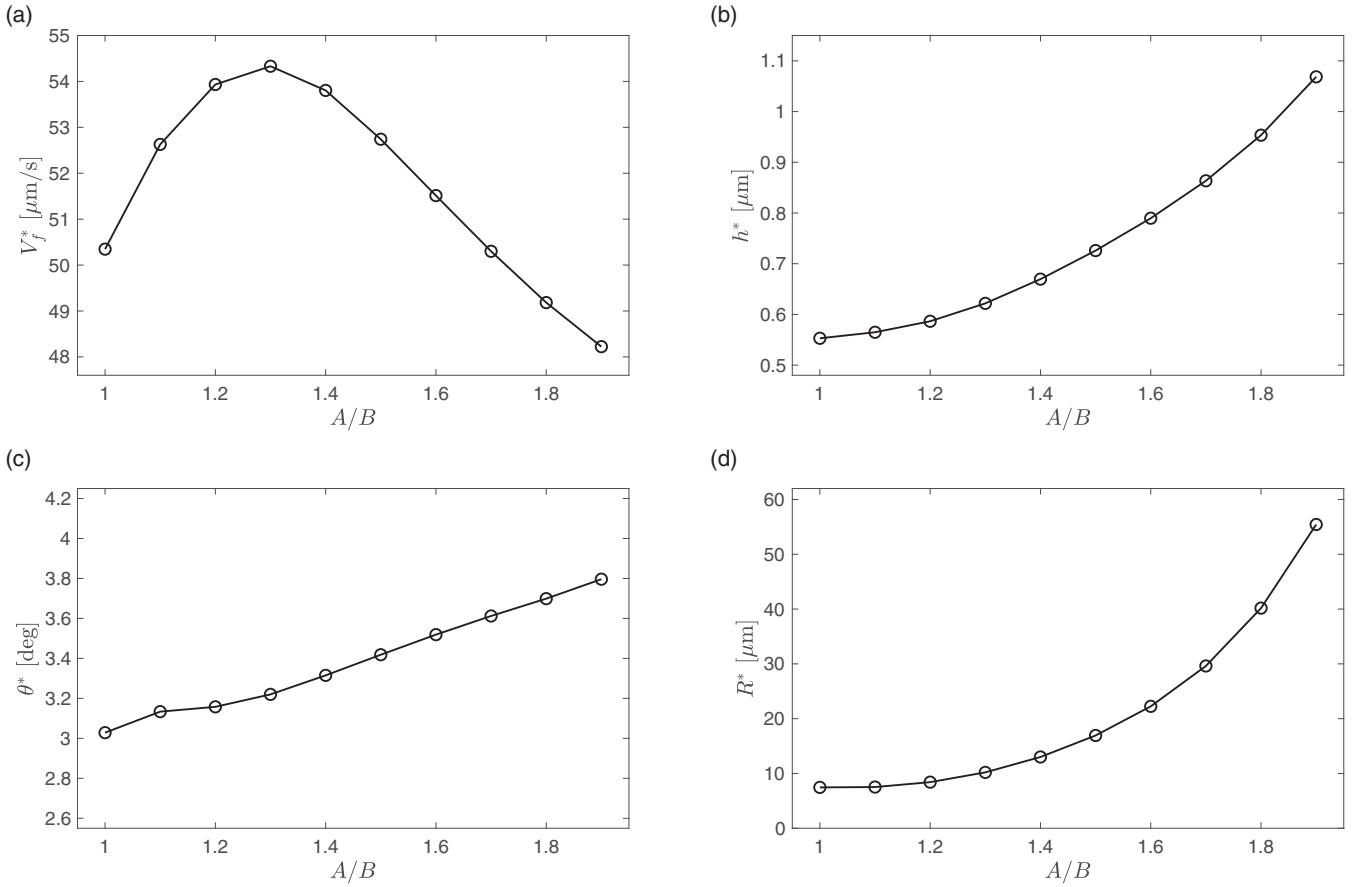

FIG. 10. Limiting values of forward swimming speed V_f^* (a), height h^* (b), inclination angle θ^* (c), and radius R^* of the circular trajectory (d) as functions of the cell body ratio A/B, while keeping $B = 0.5$ μm.

adhesion of the cells to the surface to form biofilms and microbial communities for their survival.

ACKNOWLEDGMENTS

Y.K. was supported by a National Research Foundation of Korea grant funded by the Korean government (Grant No. 2017R1E1A1A03070636). S.L. was supported by the NSF (Grant No. DMS-1853591), the SIMONS Foundation (Grant No. 585683), and the Charles Phelps Taft Research Center at the University of Cincinnati. Y.P. was supported by a National Institute for Mathematical Sciences (NIMS) grant funded by the Korea government (MSIT) (Grant No. 2019B800006).

APPENDIX

We derive the refined formula for the linear and angular velocities at any point in fluid as fundamental solutions of the regularized Stokes equations in the presence of a solid wall, which is $z = 0$.

Given a point force $\mathbf{f}_0$ and a point torque $\mathbf{n}_0$ at the point $\mathbf{X}_0$ on the boundary, the regularized Stokes equations read as follows:

$$-\nabla p + \mu\Delta\mathbf{u} + \mathbf{f}_0\psi_\delta(\mathbf{x}-\mathbf{X}_0) + \tfrac{1}{2}\nabla\times\mathbf{n}_0\psi_\delta(\mathbf{x}-\mathbf{X}_0) = 0, \tag{A1}$$

$$\nabla\cdot\mathbf{u} = 0, \tag{A2}$$

and the solution (the linear velocity) at any $\mathbf{x}$ in the free fluid space is given by

$$\mu\mathbf{u}(\mathbf{x}) = \mathcal{S}[\mathbf{f}_0] + \tfrac{1}{2}\mathcal{R}_\psi[\mathbf{n}_0], \tag{A3}$$

where $\mathcal{S}[\mathbf{f}_0]$ is the *regularized stokeslet* due to the point force $\mathbf{f}_0$ at $\mathbf{X}_0$ and $\mathcal{R}_\psi[\mathbf{n}_0]$ is the *regularized rotlet* due to the point torque $\mathbf{n}_0$ at $\mathbf{X}_0$, and they are defined as

$$\mathcal{S}[\mathbf{f}_0] = (\mathbf{f}_0\cdot\nabla)\nabla B_\psi - \mathbf{f}_0 G_\psi = \mathbf{f}_0 H_1(r) + (\mathbf{f}_0\cdot\mathbf{r})\mathbf{r}H_2(r), \tag{A4}$$

$$\mathcal{R}_\psi[\mathbf{n}_0] = \mathbf{n}_0\times\nabla G_\psi = (\mathbf{n}_0\times\mathbf{r})Q(r), \tag{A5}$$

where $\mathbf{r} = \mathbf{x}-\mathbf{X}_0$, $r = |\mathbf{r}|$, and, G_ψ and B_ψ are the regularized Green's function and biharmonic function, respectively, satisfying $\Delta G_\psi(\mathbf{r}) = \psi_\delta(\mathbf{r})$ and $\Delta B_\psi(\mathbf{r}) = G_\psi(\mathbf{r})$. Note that since the blob function $\psi_\delta(\mathbf{r})$ is radially symmetric, $G_\psi(\mathbf{r})$ and $G_\psi(\mathbf{r})$ are also radially symmetric, and thus we can write $G_\psi(r) = G_\psi(\mathbf{r})$ and $B_\psi(r) = B_\psi(\mathbf{r})$. In Eqs. (A4) and (A5), the functions H_1, H_2, and Q are defined as

$$H_1(r) = \frac{B_\psi'}{r} - G_\psi = \frac{2\delta^2+r^2}{8\pi(\delta^2+r^2)^{3/2}}, \tag{A6}$$

$$H_2(r) = \frac{rB_\psi'' - B_\psi'}{r^3} = \frac{1}{8\pi(\delta^2+r^2)^{3/2}}, \tag{A7}$$

$$Q(r) = \frac{G_\psi'}{r} = \frac{5\delta^2+2r^2}{8\pi(\delta^2+r^2)^{5/2}}. \tag{A8}$$

In order to account for the wall effect, we introduce an image point $\mathbf{X}_0^{\rm im} = (x, y, -h)$ of the boundary point $\mathbf{X}_0 = (x, y, h)$. Then we define $\mathbf{r}^* = \mathbf{x}-\mathbf{X}_0$, $\mathbf{r} = \mathbf{x}-\mathbf{X}_0^{\rm im}$, $r^* = |\mathbf{r}^*| = |\mathbf{x}-\mathbf{X}_0|$, and $r = |\mathbf{r}| = |\mathbf{x}-\mathbf{X}_0^{\rm im}|$; see Fig. 2.

In Eq. (A1), the body force acting on the fluid consists of two contributions: force and torque. Accordingly, we can divide the linear velocity $\mathbf{u}(\mathbf{x})$ into two parts and express it as

$$\mu\mathbf{u}(\mathbf{x}) = \mu\mathbf{u}_s^{\rm im}(\mathbf{x}) + \mu\mathbf{u}_r^{\rm im}(\mathbf{x}), \tag{A9}$$

where $\mathbf{u}_s^{\rm im}(\mathbf{x})$ and $\mathbf{u}_r^{\rm im}(\mathbf{x})$ are two velocities for the image system for a regularized stokeslet and a regularized rotlet, respectively. Let us first define the regularized stokeslet, denoted as $-\mathcal{S}^{\rm im}[\mathbf{f}_0]$, of strength $-\mathbf{f}_0$ at the image point $\mathbf{X}_0^{\rm im}$, then the velocity $\mathbf{u}_s^{\rm im}(\mathbf{x})$ for the image system of a regularized stokeslet is given in Ref. [29] as

$$\begin{aligned}\mu\mathbf{u}_s^{\rm im}(\mathbf{x}) = {}& \mathcal{S}[\mathbf{f}_0] - \mathcal{S}^{\rm im}[\mathbf{f}_0] + h^2\mathcal{P}[\mathbf{b}] + 2h\mathcal{D}[\mathbf{e}_3,\mathbf{b}]\\ & - 2h(\mathcal{R}_\psi[\mathbf{m}] - \mathcal{R}_\phi[\mathbf{m}]),\end{aligned} \tag{A10}$$

where $\mathbf{b} = 2(\mathbf{f}_0\cdot\mathbf{e}_3)\mathbf{e}_3 - \mathbf{f}_0$ and $\mathbf{m} = \mathbf{f}_0\times\mathbf{e}_3$. Here the *regularized potential dipole* $\mathcal{P}$ is obtained by applying the negative Laplacian to the regularized stokeslet, $-\Delta\mathcal{S}$, for a force $\tilde{\mathbf{b}}$ applied at $\mathbf{X}_0$, and thus

$$\begin{aligned}\mathcal{P}[\tilde{\mathbf{b}}] &= -(\tilde{\mathbf{b}}\cdot\nabla)\nabla(\triangle B_\phi) + \tilde{\mathbf{b}}\triangle G_\phi = -(\tilde{\mathbf{b}}\cdot\nabla)\nabla G_\phi + \tilde{\mathbf{b}}\phi_\delta\\ &= -(\tilde{\mathbf{b}}\cdot\mathbf{r})\mathbf{r}\left(\frac{rG_\phi'' - G_\phi'}{r^3}\right) - \tilde{\mathbf{b}}\left(\frac{G_\phi'}{r} - \phi_\delta\right)\\ &= -(\tilde{\mathbf{b}}\cdot\mathbf{r})\mathbf{r}D_2^\phi - \tilde{\mathbf{b}}D_1^\phi,\end{aligned} \tag{A11}$$

where G_ϕ and B_ϕ are the regularized Green's function and biharmonic function, respectively, satisfying $\Delta G_\phi(\mathbf{r}) = \phi_\delta(\mathbf{r})$ and $\Delta B_\phi(\mathbf{r}) = G_\phi(\mathbf{r})$. Then the regularized dipole functions, D_1^ϕ and D_2^ϕ, can be derived as

$$D_1^\phi(r) = \frac{G_\phi'}{r} - \phi_\delta = \frac{-2\delta^2+r^2}{4\pi(\delta^2+r^2)^{5/2}}, \tag{A12}$$

$$D_2^\phi(r) = \frac{rG_\phi'' - G_\phi'}{r^3} = \frac{-3}{4\pi(\delta^2+r^2)^{5/2}}. \tag{A13}$$

The *regularized stokeslet doublet*, $\mathcal{D}$, is the directional derivative of a regularized stokeslet, $(\tilde{\mathbf{b}}\cdot\nabla)\mathcal{S}$, in the direction of a constant vector $\tilde{\mathbf{b}}$. For a regularized stokeslet of strength $\tilde{\mathbf{a}}$, the regularized stokeslet doublet $\mathcal{D}[\tilde{\mathbf{a}},\tilde{\mathbf{b}}]$ is given by

$$\begin{aligned}\mathcal{D}[\tilde{\mathbf{a}},\tilde{\mathbf{b}}] &= (\tilde{\mathbf{b}}\cdot\nabla)\mathcal{S}[\tilde{\mathbf{a}}] = (\tilde{\mathbf{b}}\cdot\nabla)[\tilde{\mathbf{a}}H_1(r) + (\tilde{\mathbf{a}}\cdot\mathbf{r})\mathbf{r}H_2]\\ &= (\tilde{\mathbf{b}}\cdot\tilde{\mathbf{a}})\mathbf{r}H_2 + \tilde{\mathbf{b}}(\tilde{\mathbf{a}}\cdot\mathbf{r})H_2 + \tilde{\mathbf{a}}(\tilde{\mathbf{b}}\cdot\mathbf{r})\frac{H_1'}{r}\\ &\quad + (\tilde{\mathbf{b}}\cdot\mathbf{r})(\tilde{\mathbf{a}}\cdot\mathbf{r})\mathbf{r}\frac{H_2'}{r}.\end{aligned} \tag{A14}$$

Note that the constant vectors $\tilde{\mathbf{b}}$ and $\tilde{\mathbf{a}}$ are chosen to cancel the velocity on the wall in the image system.

The last term in Eq. (A10), which involves the difference of two regularized rotlets, can be written as

$$\begin{aligned}\mathcal{R}_\psi[\mathbf{m}] - \mathcal{R}_\phi[\mathbf{m}] &= \mathbf{m}\times[\nabla G_\psi - \nabla G_\phi]\\ &= \left(\frac{G_\psi'}{r} - \frac{G_\phi'}{r}\right)(\mathbf{m}\times\mathbf{r})\\ &= -H_3(\mathbf{m}\times\mathbf{r}),\end{aligned} \tag{A15}$$

where the *regularized rotlet* $\mathcal{R}_\phi[\mathbf{m}]$ is defined in the same fashion as $\mathcal{R}_\psi[\mathbf{m}]$ using the more slowly decaying blob

function $\phi_\delta(\mathbf{r})$ in Eq. (26), and the function $H_3(r)$ is defined as

$$H_3(r) = \frac{G'_\phi}{r} - \frac{G'_\psi}{r} = \frac{-3\delta^2}{8\pi(\delta^2+r^2)^{5/2}}. \tag{A16}$$

Assuming that there are N_b point forces $\mathbf{f}_k$ acted at the immersed boundary points $\mathbf{X}_k$, we can derive the explicit formula for the velocity $\mathbf{u}_s^{\text{im}}(\mathbf{x})$ given in Eq. (29) for the image system of the regularized stokeslet.

The image system for the regularized rotlet is known to be an antisymmetric part of the image system for regularized stokeslet doublet, which can be obtained by differentiating the regularized stokeslet [30]. The explicit formula for the velocity $\mathbf{u}_r^{\text{im}}(\mathbf{x})$ for the image system of a regularized rotlet, which also requires the regularized rotlet $-\mathcal{R}_\psi^{\text{im}}[\mathbf{n}_0]$ of point torque $-\mathbf{n}_0$ at the image point $\mathbf{X}_0^{\text{im}}$, has the following form [29]:

$$\begin{aligned}\mu\mathbf{u}_r^{\text{im}}(\mathbf{x}) = {}& \tfrac{1}{2}\mathcal{R}_\psi[\mathbf{n}_0] - \tfrac{1}{2}\mathcal{R}_\psi^{\text{im}}[\mathbf{n}_0] \\ & - (\mathcal{D}[\mathbf{p},\mathbf{e}_3] + \mathcal{D}[\mathbf{e}_3,\mathbf{p}] + h\mathcal{P}[\mathbf{p}]) \\ & + (\mathcal{R}_\psi[\mathbf{q}] - \mathcal{R}_\phi[\mathbf{q}]) + h(\mathcal{J}_\psi[\mathbf{n}_0,\mathbf{e}_3] - \mathcal{J}_\phi[\mathbf{n}_0,\mathbf{e}_3]) \\ & - \frac{h^2}{2}\mathcal{Q}[\mathbf{n}_0],\end{aligned} \tag{A17}$$

where $\mathbf{p} = \mathbf{n}_0 \times \mathbf{e}_3$ and $\mathbf{q} = \mathbf{n}_0 - (\mathbf{n}_0 \cdot \mathbf{e}_3)\mathbf{e}_3$.

In Eq. (A17), the *regularized rotlet doublet* $\mathcal{J}_\psi[\tilde{\mathbf{a}},\tilde{\mathbf{b}}]$ is defined as the directional derivative of a rotlet of strength $\tilde{\mathbf{a}}$ in the direction of a constant vector $\tilde{\mathbf{b}}$. Thus, for a rotlet of strength $\tilde{\mathbf{a}}$:

$$\begin{aligned}\mathcal{J}_\psi[\tilde{\mathbf{a}},\tilde{\mathbf{b}}] &= (\tilde{\mathbf{b}}\cdot\nabla)\mathcal{R}_\psi[\tilde{\mathbf{a}}] = (\tilde{\mathbf{b}}\cdot\nabla)[\tilde{\mathbf{a}}\times\nabla G_\psi] \\ &= (\tilde{\mathbf{b}}\cdot\mathbf{r})(\tilde{\mathbf{a}}\times\mathbf{r})\left(\frac{rG''_\psi - G'_\psi}{r^3}\right) + \frac{G'_\psi}{r}(\tilde{\mathbf{a}}\times\tilde{\mathbf{b}}).\end{aligned} \tag{A18}$$

We can similarly define the *regularized rotlet doublet* $\mathcal{J}_\phi[\tilde{\mathbf{a}},\tilde{\mathbf{b}}]$ as

$$\mathcal{J}_\phi[\tilde{\mathbf{a}},\tilde{\mathbf{b}}] = (\tilde{\mathbf{b}}\cdot\mathbf{r})(\tilde{\mathbf{a}}\times\mathbf{r})\left(\frac{rG''_\phi - G'_\phi}{r^3}\right) + \frac{G'_\phi}{r}(\tilde{\mathbf{a}}\times\tilde{\mathbf{b}}). \tag{A19}$$

The *regularized quadrupole* $\mathcal{Q}[\tilde{\mathbf{c}}]$ is obtained by applying the negative curl to the dipole, $-\nabla\times\mathcal{P}$, of strength $\tilde{\mathbf{c}}$:

$$\begin{aligned}\mathcal{Q}[\tilde{\mathbf{c}}] &= -\nabla\times\mathcal{P}[\tilde{\mathbf{c}}] = \nabla\times\left[(\tilde{\mathbf{c}}\cdot\mathbf{r})\mathbf{r}D_2^\phi + \tilde{\mathbf{c}}D_1^\phi\right] \\ &= \left[D_2^\phi - \frac{(D_1^\phi)'}{r}\right](\tilde{\mathbf{c}}\times\mathbf{r}) = -2H_4(\tilde{\mathbf{c}}\times\mathbf{r}),\end{aligned} \tag{A20}$$

where H_4 is defined as

$$H_4(r) = \frac{(D_1^\phi)'}{2r} - \frac{D_2^\phi}{2} = \frac{15\delta^2}{8\pi(\delta^2+r^2)^{7/2}}. \tag{A21}$$

In order to derive and simplify the formula for the linear and angular velocities of the image system, we here introduce some important identities. To do that, we first define the following two functions:

$$D_1^\psi(r) = \frac{G'_\psi}{r} - \psi_\delta = \frac{-10\delta^4 + 7r^2\delta^2 + 2r^4}{8\pi(\delta^2+r^2)^{7/2}}, \tag{A22}$$

$$D_2^\psi(r) = \frac{rG''_\psi - G'_\psi}{r^3} = \frac{-21\delta^2 - 6r^2}{8\pi(\delta^2+r^2)^{7/2}}. \tag{A23}$$

Then we can show the following identities by the direct computations:

$$\frac{H'_2}{r} = \frac{D_2^\phi}{2}, \tag{A24}$$

$$Q = \frac{G'_\psi}{r} = H_2 - \frac{H'_1}{r}, \tag{A25}$$

$$H_3 = \frac{G'_\phi}{r} - \frac{G'_\psi}{r} = \frac{H'_1}{r} + H_2 = \frac{1}{2}D_1^\phi - H_2, \tag{A26}$$

$$H_4 = \frac{(D_1^\phi)'}{2r} - \frac{D_2^\phi}{2} = \frac{H'_3}{r} = D_2^\phi - D_2^\psi. \tag{A27}$$

Assuming that there are N_b point torques $\mathbf{n}_k$ acted at the boundary points $\mathbf{X}_k$, we can derive the explicit formula for the velocity $\mathbf{u}_r^{\text{im}}(\mathbf{x})$ given in Eq. (29) from Eq. (A17) with the help of the following two simplified equations:

$$\begin{aligned}\mathcal{D}[\mathbf{p},\mathbf{e}_3] + \mathcal{D}[\mathbf{e}_3,\mathbf{p}] &= [(\mathbf{e}_3\cdot\mathbf{r})\mathbf{p} + (\mathbf{p}\cdot\mathbf{r})\mathbf{e}_3]\left(\frac{H'_1}{r} + H_2\right) + 2(\mathbf{e}_3\cdot\mathbf{r})(\mathbf{p}\cdot\mathbf{r})\mathbf{r}\frac{H'_2}{r} \\ &= [(\mathbf{e}_3\cdot\mathbf{r})\mathbf{p} + (\mathbf{p}\cdot\mathbf{r})\mathbf{e}_3]H_3 + (\mathbf{e}_3\cdot\mathbf{r})(\mathbf{p}\cdot\mathbf{r})\mathbf{r}D_2^\phi,\end{aligned} \tag{A28}$$

$$\begin{aligned}\mathcal{J}_\psi[\mathbf{n}_0,\mathbf{e}_3] - \mathcal{J}_\phi[\mathbf{n}_0,\mathbf{e}_3] &= (\mathbf{e}_3\cdot\mathbf{r})(\mathbf{n}_0\times\mathbf{r})\left(D_2^\psi - D_2^\phi\right) + \left(\frac{G'_\psi}{r} - \frac{G'_\phi}{r}\right)(\mathbf{n}_0\times\mathbf{e}_3) \\ &= -(\mathbf{r}\cdot\mathbf{e}_3)(\mathbf{n}_0\times\mathbf{r})H_4 - \mathbf{p}H_3.\end{aligned} \tag{A29}$$

The previous models in Refs. [29,30] have described and used only the linear velocity in the image system given in Eq. (29). Here we provide the detailed formula for the angular velocity in the image system since our model requires the angular velocity to rotate the orthonormal triad $\{\mathbf{D}^1(s,t), \mathbf{D}^2(s,t), \mathbf{D}^3(s,t)\}$ along the flagellum. (For the derivation of the angular velocity in a free space, see Ref. [25].) Since the angular velocity can be computed by taking curl on the linear velocity, which is composed of the image systems of the regularized stokeslet and rotlet, we can write

$$\mu\mathbf{w}^{\text{im}}(\mathbf{x}) = \mu\mathbf{w}_s^{\text{im}}(\mathbf{x}) + \mu\mathbf{w}_r^{\text{im}}(\mathbf{x}) = \tfrac{1}{2}\nabla\times\mu\mathbf{u}_s^{\text{im}}(\mathbf{x}) + \tfrac{1}{2}\nabla\times\mu\mathbf{u}_r^{\text{im}}(\mathbf{x}), \tag{A30}$$

and we have to know only how to take curl on all the terms composing the linear velocity $\mathbf{u}^{\text{im}}(\mathbf{x})$. We state all the components needed to compute the angular velocity from the image system of the regularized stokeslet $\mathbf{u}_s^{\text{im}}(\mathbf{x})$ and regularized rotlet $\mathbf{u}_r^{\text{im}}(\mathbf{x})$

as follows:

$$\frac{1}{2}\nabla\times\mathcal{S}[\mathbf{f}_0]=\frac{1}{2}\nabla\times[\mathbf{f}_0H_1(r^*)+(\mathbf{f}_0\cdot\mathbf{r}^*)\mathbf{r}^*H_2(r^*)]=\frac{1}{2}\left[H_2(r^*)-\frac{H_1'(r^*)}{r}\right](\mathbf{f}_0\times\mathbf{r}^*)=\frac{1}{2}Q(r^*)(\mathbf{f}_0\times\mathbf{r}^*),$$

$$-\frac{1}{2}\nabla\times\mathcal{S}^{\rm im}[\mathbf{f}_0]=-\frac{1}{2}Q(\mathbf{f}_0\times\mathbf{r}),$$

$$\frac{1}{2}\nabla\times(h^2\mathcal{P}[\mathbf{b}])=\frac{h^2}{2}\nabla\times\left[-\mathbf{b}D_1^\phi-(\mathbf{b}\cdot\mathbf{r})\mathbf{r}D_2^\phi\right]=\frac{h^2}{2}\left[\frac{\left(D_1^\phi\right)'}{r}-D_2^\phi\right](\mathbf{b}\times\mathbf{r})=h^2\,H_4(\mathbf{b}\times\mathbf{r}),$$

$$\begin{aligned}\frac{1}{2}\nabla\times(2h\mathcal{D}[\mathbf{e}_3,\mathbf{b}])&=h\nabla\times\left[(\mathbf{b}\cdot\mathbf{e}_3)\mathbf{r}H_2+\mathbf{b}(\mathbf{e}_3\cdot\mathbf{r})H_2+\mathbf{e}_3(\mathbf{b}\cdot\mathbf{r})\frac{H_1'}{r}+(\mathbf{b}\cdot\mathbf{r})(\mathbf{e}_3\cdot\mathbf{r})\mathbf{r}\frac{H_2'}{r}\right]\\&=h\left(H_2-\frac{H_1'}{r}\right)\mathbf{m}+h\left[\frac{H_2'}{r}-\left(\frac{H_1}{r}\right)'\frac{1}{r}\right](\mathbf{b}\cdot\mathbf{r})(\mathbf{e}_3\times\mathbf{r})=hQ\mathbf{m}+h\left(D_2^\phi-H_4\right)(\mathbf{b}\cdot\mathbf{r})(\mathbf{e}_3\times\mathbf{r}),\end{aligned}$$

$$\frac{1}{2}\nabla\times\{-2h(\mathcal{R}_\psi[\mathbf{m}]-\mathcal{R}_\phi[\mathbf{m}])\}=\frac{1}{2}\nabla\times[2hH_3(\mathbf{m}\times\mathbf{r})]=h[(r^2H_4+2H_3)\mathbf{m}-H_4(\mathbf{m}\cdot\mathbf{r})\mathbf{r}],$$

$$\begin{aligned}\frac{1}{2}\nabla\times\frac{1}{2}\mathcal{R}_\psi[\mathbf{n}_0]&=\frac{1}{4}\nabla\times[(\mathbf{n}_0\times\mathbf{r}^*)Q(r^*)]=\frac{1}{4}[2Q(r^*)+r^*Q'(r^*)]\mathbf{n}_0-\frac{1}{4}\frac{Q'(r^*)}{r}(\mathbf{n}_0\cdot\mathbf{r}^*)\mathbf{r}^*\\&=-\frac{1}{4}D_1^\psi(r^*)\mathbf{n}_0-\frac{1}{4}D_2^\psi(r^*)(\mathbf{n}_0\cdot\mathbf{r}^*)\mathbf{r}^*-\frac{1}{2}\nabla\times\mathcal{R}_\psi^{\rm im}[\mathbf{n}_0]=\frac{1}{4}D_1^\psi\mathbf{n}_0+\frac{1}{4}D_2^\psi(\mathbf{n}_0\cdot\mathbf{r})\mathbf{r},\end{aligned}$$

$$\begin{aligned}\frac{1}{2}\nabla\times(-\mathcal{D}[\mathbf{p},\mathbf{e}_3]-\mathcal{D}[\mathbf{e}_3,\mathbf{p}])&=-\frac{1}{2}\nabla\times\left\{[(\mathbf{e}_3\cdot\mathbf{r})\mathbf{p}+(\mathbf{p}\cdot\mathbf{r})]\mathbf{e}_3H_3+(\mathbf{e}_3\cdot\mathbf{r})(\mathbf{p}\cdot\mathbf{r})\mathbf{r}D_2^\phi\right\}\\&=-\frac{1}{2}\left(D_2^\phi-H_4\right)[(\mathbf{e}_3\cdot\mathbf{r})(\mathbf{p}\times\mathbf{r})+(\mathbf{p}\cdot\mathbf{r})(\mathbf{e}_3\times\mathbf{r})],\end{aligned}$$

$$\frac{1}{2}\nabla\times(-h\mathcal{P}[\mathbf{p}])=-hH_4(r)(\mathbf{p}\times\mathbf{r}),$$

$$\frac{1}{2}\nabla\times(\mathcal{R}_\psi[\mathbf{q}]-\mathcal{R}_\phi[\mathbf{q}])=-\frac{1}{2}\nabla\times[(\mathbf{q}\times\mathbf{r})H_3]=-\frac{1}{2}(r^2H_4+2H_3)\mathbf{q}+\frac{1}{2}H_4(\mathbf{q}\cdot\mathbf{r})\mathbf{r},$$

$$\begin{aligned}\frac{1}{2}\nabla\times h(\mathcal{J}_\psi[\mathbf{n}_0,\mathbf{e}_3]-\mathcal{J}_\phi[\mathbf{n}_0,\mathbf{e}_3])&=-\frac{h}{2}\nabla\times[(\mathbf{r}\cdot\mathbf{e}_3)(\mathbf{n}_0\times\mathbf{r})H_4+\mathbf{p}H_3]\\&=-\frac{h}{2}\{(\mathbf{r}\cdot\mathbf{e}_3)(3H_4+r^2H_5)\mathbf{n}_0-[(\mathbf{n}_0\cdot\mathbf{e}_3)H_4+(\mathbf{r}\cdot\mathbf{e}_3)(\mathbf{n}_0\cdot\mathbf{r})H_5]\,\mathbf{r}-(\mathbf{p}\times\mathbf{r})H_4\},\end{aligned}$$

$$\frac{1}{2}\nabla\times\left(-\frac{h^2}{2}\mathcal{Q}[\mathbf{n}_0]\right)=\frac{h^2}{2}\nabla\times[(\mathbf{n}_0\times\mathbf{r})H_4]=\frac{h^2}{2}[(2H_4+r^2H_5)\mathbf{n}_0-H_5(\mathbf{n}_0\cdot\mathbf{r})\mathbf{r}],$$

where H_5 is defined as

$$H_5(r)=\frac{H_4'}{r}=\frac{-105\delta^2}{8\pi(r^2+\delta^2)^{9/2}}.\tag{A31}$$

In the above equations, all the single variable functions are evaluated at r when there is no indication of the independent variable. When we have N_b point forces $\mathbf{f}_k$ and N_b point torques $\mathbf{n}_k$ centered at the boundary points $\mathbf{X}_k$, $k=1,\ldots,N_b$, we can apply the resulting fundamental solutions (kernels) to derive the angular velocity $\mathbf{w}^{\rm im}(\mathbf{x})$, which is given in Eq. (30).

[1] H. C. Berg, Annu. Rev. Biochem. **72**, 19 (2003).
[2] H. C. Berg and R. A. Anderson, Nature (London) **245**, 380 (1973).
[3] S. Chattopadhyay and X.-L. Wu, Biophys. J. **96**, 2023 (2009).
[4] E. Lauga and T. R. Powers, Rep. Prog. Phys. **72**, 096601 (2009).

[5] E. Lauga, Annu. Rev. Fluid Mech. **48**, 105 (2016).
[6] E. M. Purcell, Proc. Natl. Acad. Sci. USA **94**, 11307 (1997).
[7] M. Ramia, K. L. Tullock, and N. Phan-Thien, Biophy. J. **65**, 755 (1993).
[8] A. Sen, R. K. Nandy, and A. N. Ghosh, J. Electron. Microsc. **53**, 305 (2004).
[9] R. Stocker, Proc. Natl. Acad. Sci. USA **108**, 2635 (2011).
[10] H. C. Berg and L. Turner, Biophys. J. **58**, 919 (1990).
[11] P. D. Frymier, R. M. Ford, H. C. Berg, and P. T. Cummings, Proc. Natl. Acad. Sci. USA **92**, 6195 (1995).
[12] M. A. Vigeant and R. M. Ford, Appl. Environ. Microbiol. **63**, 3474 (1997).
[13] L. A. Pratt and R. kolter, Mol. Microbiol. **30**, 285 (1998).
[14] G. O'Toole, H. B. Kaplan, and R. Kolter, Annu. Rev. Microbiol. **54**, 49 (2000).
[15] R. Rusconi, S. Lecuyer, L. Guglielmini, and H. A. Stone, J. R. Soc. Interface **7**, 1293 (2010).
[16] D. Giacché, T. Ishikawa, and T. Yamaguchi, Phys. Rev. E **82**, 056309 (2010).
[17] S. Kudo, N. Imai, M. Nishitoba, S. Sugiyama, and Y. Magariyama, FEMS Microbiol. Lett. **242**, 221 (2005).
[18] Y. Magariyama, M. Ichiba, K. Nakata, K. Baba, T. Ohtani, S. Kudo, and T. Goto, Biophys. J. **88**, 3648 (2005).
[19] A. J. Reynolds, J. Fluid. Mech. **23**, 241 (1965).
[20] E. Lauga, W. R. DiLuzio, G. M. Whitesides, and H. A. Stone, Biophys J. **90**, 400 (2006).
[21] H. Shum, E. A. Gaffney, and D. J. Smith, Proc. R. Soc. A **466**, 1725 (2010).
[22] S. V. Srigiriraju and T. R. Powers, Phys. Rev. E **73**, 011902 (2006).
[23] H. Hotani, J. Mol. Biol. **156**, 791 (1982).
[24] R. Vogel and H. Stark, Phys. Rev. Lett. **110**, 158104 (2013).
[25] S. Lim, A. Ferent, X. S. Wang, and C. S. Peskin, SIAM J. Sci. Comput. **31**, 273 (2008).
[26] S. Olson, S. Lim, and R. Cortez, J. Comp. Phys. **238**, 169 (2013).
[27] W. Lee, Y. Kim, S. D. Olson, and S. Lim, Phys. Rev. E **90**, 033012 (2014).
[28] Y. Kim and C. S. Peskin, Phys. Fluids **28**, 033603 (2016).
[29] J. Ainley, S. Durkin, R. Embid, P. Boindala, and R. Cortez, J. Comp. Phys. **227**, 4600 (2008).
[30] R. Cortez and D. Varela, J. Comp. Phys. **285**, 41 (2015).
[31] Y. Park, Y. Kim, and S. Lim, J. Fluid Mech. **859**, 586 (2019).
[32] J. J. Higdon, J. Fluid Mech. **94**, 331 (1979).
[33] R. Cortez, SIAM J. Sci. Comput. **23**, 1204 (2001).
[34] S. Lim and C. S. Peskin, Phys. Rev. E **85**, 036307 (2012).
[35] J. R. Blake, Math. Proc. Camb. Philos. Soc. **70**, 303 (1971).
[36] See Supplemental Material at http://link.aps.org/supplemental/10.1103/PhysRevE.100.063112 for simulation movies.